International Journal of Mechanical Sciences 313 (2026) 111291

Contents lists available at ScienceDirect

International Journal of Mechanical Sciences

journal homepage: www.elsevier.com/locate/ijmecsci

# Hierarchical physics-guided neural network for sparse-data heterogeneous material identification

Kunpeng Xu [b], Ning Zhang [a,b,*], Zhen-Yu Yin [b,*], Kai-Qi Li [a,b]

[a] Wuhan University, Wuhan, Hubei 430072, China
[b] Department of Civil and Environmental Engineering, The Hong Kong Polytechnic University, Hung Hom, Kowloon, Hong Kong

ARTICLE INFO

*Keywords:*
Physics-informed neural network
Finite element method
Inverse analysis
Heterogeneous material properties identification
Hierarchical physics-guided strategy
Sparse data inverse identification

ABSTRACT

Physics-informed neural networks (PINNs) have garnered increasing attention in computational solid mechanics for their potential in inverse problem solving. However, conventional PINNs often suffer from slow convergence and suboptimal accuracy when identifying heterogeneous material properties, especially under sparse data labels. To overcome these limitations, this paper proposes a novel hierarchical physics-guided neural network (HPGNN) framework for efficient and accurate inverse identification of heterogeneous material properties using only sparse observational data. In HPGNN, all unknown domain-wise parameters are embedded as trainable variables within the neural network, enabling a seamless integration of finite element method (FEM)-based domain discretization with neural network–driven inverse parameter identification. The hierarchical strategy progressively reconstructs the heterogeneous material field from coarse to fine scales, ensuring both global consistency and local accuracy under sparse supervision. To improve practical convergence robustness, an LBFGS restart mechanism is incorporated to overcome optimization stagnation, markedly accelerating convergence compared with traditional training schemes. A series of validation experiments are conducted and demonstrate that HPGNN achieves high computational efficiency and low error level cross multiple random field realizations. Additional investigations considering random-input perturbations, extreme initial guesses, variations in mesh resolution, and label noise further confirm the robustness of the proposed framework. A direct comparison with an operator-learning baseline (DeepONet) highlights the advantage of HPGNN inversion under sparse data condition, achieving lower reconstruction error. This study highlights the potential of HPGNN for further development and practical applications in the heterogeneous materials inverse analysis.

## 1. Introduction

Identifying material properties is essential for predicting mechanical responses and assessing damage risks, which are critical for the safety and design of various engineering applications, such as slope engineering, foundations, and advanced manufacturing [1–7]. For homogeneous materials, typically only one parameter needs to be identified, as the material properties are consistent throughout the domain. For traditional numerical methods, such as the finite element method (FEM) [8–13], finite difference method (FDM) [14–17], material point method (MPM) [18–22], and discrete element method (DEM) [23–26], determining material parameters in inverse analysis often relies on external optimization techniques, such as adjoint methods, which require solving the full forward problem at each iteration. In addition to numerical simulation, the remaining option is to conduct extensive experiments [27–29]. This leads to high computational costs and reduced efficiency [30,31]. For materials with random properties varying spatially in a stochastic manner, the inverse analysis becomes a high-dimensional problem, posing significant challenges for traditional approaches.

Recently, attempts have been made to leverage deep learning (DL) methods as an alternative modeling paradigm to traditional numerical analysis [32–36]. DL is developing at an unprecedented speed and is increasingly being applied in various disciplines [37–44], such as slope analysis [45], large language model-based geotechnical design [46–49], soil property prediction [50–52], constitutive models [53,54]. Generally, purely data-driven DL models excel in supervised learning tasks with abundant labeled data, while their performance degrades significantly in scenarios with limited data, which is often encountered in

* Corresponding authors.
*E-mail addresses:* kun-peng.xu@connect.polyu.hk (K. Xu), ning-cee.zhang@polyu.edu.hk (N. Zhang), zhenyu.yin@polyu.edu.hk (Z.-Y. Yin), kqcee.li@polyu.edu.hk (K.-Q. Li).

https://doi.org/10.1016/j.ijmecsci.2026.111291
Received 1 October 2025; Received in revised form 17 December 2025; Accepted 18 January 2026
Available online 18 January 2026

engineering applications due to high data acquisition costs [55]. DL methods with physics constraints, such as physics-informed neural networks (PINNs) proposed by Raissi et al., have emerged as a more promising solution due to their ability to combine physics laws and data [56–58]. However, PINNs still face several inherent challenges that hinder their broader applicability. One of the limitations is their relatively weak enforcement of physical constraints [59,60]. In conventional PINNs, the loss function is constructed using automatic differentiation (AD) to compute the residuals of governing equations only at discrete collocation points [61,62]. It fails to incorporate information from neighboring points and thus overlooks the conservation relationships that exist across the spatial domain [63]. In addition, PINNs often suffer from instability and slow or poor convergence during training [64,65]. The optimization is typically highly non-convex, making the training process complicated. This challenge frequently leads to training stagnation or convergence to suboptimal solutions.

In recent years, researchers have increasingly explored the integration of traditional numerical methods such as finite volume method (FVM), FEM, FDM into the PINN framework. For example, Wei, et al. [66] proposes a fast finite volume enhanced PINN (FFV-PINN) that stabilizes training and accelerates convergence by incorporating simplified finite volume method (FVM) and residual correction loss, enabling data-free solutions to high-Reynolds and high Rayleigh flow problems with significantly improved speed. Liu, et al. [67] introduces a framework of the nonlinear finite element based on hierarchical deep-learning neural network (HiDeNN) approximation (nonlinear HiDeNN-FEM) that uses partial derivative operator block, r-adaptivity block, and material derivative blocks to enhance finite element accuracy, reduce element distortion, and suppress hourglass modes, outperforming conventional FEM in 2D and 3D examples. Jiang, et al. [68] proposes finite difference-based PINNs (FD-PINNs) for the steady incompressible flow simulation. The results demonstrate that FD-PINNs achieve improvements in accuracy, training convergence, and computational efficiency compared with AD-PINNs. Moreover, when solving high-Re cavity flow with insufficient mesh points, FD-PINNs outperform conventional flow solvers. By incorporating these well-established approaches, derivative terms in partial differential equations (PDEs) can be approximated using structured discretization schemes. This integration can strengthen the spatial coupling among collocation points and enhances the ability of PINNs to capture the physical relationships embedded within the governing equations. In inverse analysis, Haghighat et al. introduced the application of PINNs in solid mechanics inversion and proxy modeling [69]. In addition, Wang et al. proposed Kolmogorov-Arnold-informed neural networks which demonstrate significant advantages in solving inverse problems of complex functions by incorporating KAN into the strong, energy and inverse forms of PDEs [42]. This method has the lowest relative error of 5.53 % in solving the thermal conductivity inverse problem for famous paintings. Badia et al. introduced finite element interpolated neural networks to solve the inverse problem using a cost-effective initialization and one-loop algorithm, eliminating the need for a regularization term [31]. Physics-informed deep learning method developed by Guo and Yin can effectively address inverse problems in consolidation analysis with less training data and become a versatile alternative modeling tool in geotechnical engineering [70]. Xu et al. presented a multi-task learning method using uncertainty weighting with a transfer learning strategy to improve both training efficiency and accuracy of PINN linear elastic and hyper elastic inverse problems, which can be applied to different structural loading scenarios [71]. Motlagh et al. proposed a computationally efficient inverse material characterization using PINN based on partial field response measurements [72]. Numerous computational methods based on PINNs have been developed to tackle diverse practical inverse problems. Each method offers distinct advantages and faces specific limitations, with its effectiveness being largely determined by the specific requirements of the problem at hand [73]. In recent years, inverse analysis methods have received growing attention for identifying material parameters, especially in heterogeneous materials with limited experimental data [74–79]. Compared with the inverse analysis of homogeneous cases based on deterministic mathematical models, the inverse analysis of heterogeneous materials remains challenging due to their irregular spatial variability [80]. Recent studies have explored resolution-independent or uncertainty-aware inverse frameworks based on operator learning to solve multi-parameter inverse problems and spatially heterogeneous inverse problems. Wang, et al. [81] proposed an Approximate Bayesian Computation (ABC) with a DeepONet-based Resolution Independent Strategy (DRIS) to inversely determine material parameters in the Heat-Affected Zone (HAZ) of welded joints. In their approach, the parameter, spatial coordinates and force-displacement responses are treated as a functional mapping and learned using DeepONet. The coordinate is explicitly included as input, enabling direct handling of misaligned snapshots without requiring point-wise alignment through preprocessing algorithms such as interpolation. Once the operator mapping is learned, the response can be evaluated at any location within the domain for a given set of parameters, thereby achieving resolution independence and motivating the DRIS. Jiang, et al. [82] further proposed a resolution-independent operator learning-based generative adversarial network (OL-GAN). The OL-GAN learning a functional mapping for the joint distribution of unknown parameters and system responses, enabling efficient Bayesian inference in a low-dimensional latent space, thereby alleviating the challenges of prior selection and expensive computational cost. Jiang, et al. [83] proposed an ensemble physics-informed neural network (E-PINN) to handle function estimation and uncertainty quantification of space-dependent inverse heat conduction problems (IHCPs). To enhance robustness under noisy observations, adversarial training (AT) is also incorporated as a regularization mechanism. Moreover, they develop an uncertainty-driven adaptive active sampling strategy (AS) that sequentially adds new measurements at locations with maximum variance and stops when the maximum uncertainty falls below a threshold value, enhancing the accuracy of material field inversion. Wang, et al. [84] proposed a data-driven-based approximate Bayesian computation (ABC) inverse method to quantify uncertainties of fiber path parameters in variable stiffness composite laminates. In their framework, an auto-encoder (AE) is employed to extract low-dimensional feature vectors from high-dimensional displacement fields as summary statistics for ABC, alleviating the difficulty of manual statistic selection. In addition, back-propagation neural network is used to construct a mapping between path parameters and the feature vectors, avoiding repeated simulations. A hybrid adaptive nested sampling strategy is also proposed to accelerate posterior sampling. While the above studies mainly focus on operator learning, they generally rely on the availability of extensive prior datasets to construct data-driven functional mappings between parameters and responses. These approaches are effective when rich information is accessible, enabling the learning of resolution-independent operators. However, in many practical engineering inverse problems, especially in geotechnical applications, such prior datasets are unavailable. The inverse analysis must be performed for a single engineering instance, where material properties are unknown and only sparse response measurements are accessible. In this case, constructing data-driven mappings becomes highly challenging due to the lack of prior knowledge and the high dimensionality of spatially heterogeneous parameters.

To address this challenge, this study proposes a novel hierarchical physics-guided neural network (HPGNN) framework for inverse analysis of heterogeneous material properties based on sparse data. By integrating the complete finite element formulation with a hierarchical strategy, the proposed framework avoids the need for large training datasets and instead leverages physical constraints to control the conditioning and scalability of high-dimensional inverse problems, enabling stable and accurate identification under sparse observations. It should be emphasized that the hierarchical strategy adopted in this work is different from existing multi-fidelity or progressive PINN approaches,

both in its objective and in the type of inverse problem it addresses. For example, Meng and Karniadakis [85] developed physics-informed neural networks to be trained with multi-fidelity data sets (MPINNs), primarily focus on leveraging low- and high-fidelity datasets to improve solution accuracy under limited high-fidelity data, In their framework, the unknown physical parameters are typically low-dimensional. In addition, Yang, et al. [86] proposes a PINN architecture based on the concept of progressive training and trainable weights to improve convergence in strongly nonlinear inverse problems. However, the unknowns in this study correspond to global functional mappings rather than spatially distributed parameters. Furthermore, Yang, et al. [87] introduced Adaptive Task Decomposition Physics-Informed Neural Networks (ATD-PINNs) to improve the training stability of PINNs for forward PDE problems. This framework progressively activates loss terms or residual subsets while keeping the dimensionality of the unknown solution fixed. In contrast to the above approaches, the hierarchical strategy adopted in the HPGNN framework is specifically designed to address the conditioning and scalability challenges arising in inverse identification of spatially heterogeneous material fields. When the material properties are discretized at the element level, direct inversion on a fine mesh leads to curse of dimensionality. The proposed hierarchical strategy mitigates this issue by controlling the effective dimensionality of the inverse problem, thereby enabling stable identification under sparse observations. Through a series of systematic numerical experiments, we demonstrate that HPGNN is capable of efficiently and accurately identifying material properties in heterogeneous domains under sparse data. The results further indicate that this framework exhibits strong robustness when subjected to measurement noise.

This paper is organized as follows: Section 2 details the structure and algorithm of the proposed HPGNN framework and introduces the fundamental theories of random fields. Section 3 presents numerical experiments to validate the effectiveness of HPGNN. In Section 4, extensive investigations are carried out to assess the robustness and efficiency of the proposed framework, including the impacts of random input perturbations, the LBFGS restart mechanism, noise sensitivity, and the feasibility of direct computation. A comparative study with DeepONet approaches is also conducted. Finally, Section 5 summarizes the main conclusions.

## 2. Methodology

### 2.1. Proposed HPGNN framework

This section presents the framework of Hierarchical Physics-Guided Neural Network (HPGNN). In this framework, physics guidance refers to the direct embedding of the governing equations of the FEM and the associated field responses into the neural network. In this way, heterogeneous materials are discretized into distinct domains where physical constraints are enforced, with the neural network is tasked with parameter identification at the domain level. Notably, the framework is designed to operate under sparse-data conditions, where only limited observation points with displacement and force information are available. Instead of relying on dense point-wise data, the framework identifies material properties at the domain scale, thereby yielding a sparse yet physically meaningful representation of the random field. In this study, spatial random fields with prescribed Gaussian covariance functions are employed to represent heterogeneous geomaterial properties. This covariance function with its associated hyperparameters is assumed to be known as a priori and are therefore not treated as unknowns in the inverse analysis. This work focuses on evaluating the ability of the proposed framework to recover heterogeneous material properties from limited observations.

Specifically, the nodes of FEM-discretized domain serve as the collocation points for the PINN, while the constitutive model matrix [$\boldsymbol{D}$] and the strain-displacement matrix [$\boldsymbol{B}$], both derived from FEM, are employed to compute strains and stresses. The material parameters of each domain are embedded as trainable variables, which directly define the form of the [$\boldsymbol{D}$]. This matrix is subsequently used to assemble the force equilibrium equations, which constitute a component of the loss function. Through this linkage, optimizing the trainable parameters enforces consistency between neural network predictions and the FEM-based physical constraints. This framework mitigates two major limitations of traditional PINNs: (1) the expensive computational cost associated with automatic differentiation, especially in solving PDEs with high-order derivatives [88]; and (2) the demand for a large number of collocation points to ensure accuracy, which can significantly increase the training burden [89].

The term 'Hierarchical' refers to a two-stage inverse identification strategy that progressively refines material property estimation, first capturing global trends and then resolving local details. In stage one, the entire domain is discretized into a small number of coarse elements, and the material properties of these coarse elements are defined as trainable parameters. Optimized using sparse observation labels, these coarse-scale properties approximate the average material parameters within each region, which represent the aggregated properties of multiple original fine-scale mesh elements. These resulting coarse scale random fields can then be interpolated back onto the original mesh to approximate the distribution of the true material random field under sparse-data constraints. In stage two, a local refinement strategy is applied. One of the coarse elements is further subdivided into finer elements, while the remaining elements retain their stage one material properties without further updated. The material properties obtained in stage one serve as the initial values for refined training, enabling more focused and efficient optimization under sparse-data conditions. Iteratively, all coarse elements are refined, yielding fine-scale distributions of material properties for each domain. These refined results can again be interpolated onto the original mesh to approximate the detailed spatial distribution of the heterogeneous material properties. The overall architecture of the HPGNN framework is illustrated in Fig. 1.

As shown in Fig. 1, the study domain is discretized using FEM, and the nodal coordinates are input into a deep neural network (DNN) to predict the unknown nodal displacement field.

$$\boldsymbol{u^{NN}} = \left(\boldsymbol{u_x}^{\boldsymbol{nn}}, \boldsymbol{u_y}^{\boldsymbol{nn}}\right) = \boldsymbol{DNN}(\boldsymbol{x}, \boldsymbol{y} \mid \boldsymbol{W}). \tag{1}$$

Based on the predicted displacements, the strain and stress at the Gaussian integration points are computed through the strain-displacement matrix [$\boldsymbol{B}$] and the constitutive matrix [$\boldsymbol{D}$]. Subsequently, the nodal force $F^{NN}$ can be calculated:

$$\begin{aligned} &\left\{\varepsilon_{Gauss}^{NN}\right\} = [\boldsymbol{B}]\left\{u^{NN}\right\}, \\ &\left\{\sigma_{Gauss}^{NN}\right\} = [\boldsymbol{D}]\left\{\varepsilon_{Gauss}^{NN}\right\}, \\ &\boldsymbol{F^{NN}} = \int\int \boldsymbol{B^T \sigma_G^{NN}} \boldsymbol{dxdy}. \end{aligned} \tag{2}$$

The weak form of the governing equations is established using Gaussian quadrature and incorporated into the loss function. In addition to the weak form loss, the overall loss function is constructed in the same manner as in the traditional PINN framework, as shown below:

$$\begin{aligned} &\mathscr{L}_1 = \mathscr{L}_{eq}\left(F^{NN}, F^{s}\right), \\ &\mathscr{L}_2 = \mathscr{L}\left(F^{NN}, F^{True}\right), \\ &\mathscr{L}_3 = \mathscr{L}\left(\Gamma^{NN}, \Gamma^{True}\right), \\ &\mathscr{L}_4 = \mathscr{L}_{\Gamma}\left(u^{NN}, u^{True}\right), \\ &\mathscr{L} = w_1\mathscr{L}_1 + w_2\mathscr{L}_2 + w_3\mathscr{L}_3 + w_4\mathscr{L}_4, \end{aligned} \tag{3}$$

where $F_s$ is the body force, $F^{True}$ denotes the label force, $\Gamma$ is the boundary condition, $u^{True}$ represents the label displacement, $w_1$, $w_2$, $w_3$ and $w_4$ are the weighting coefficients of each loss function in this framework. In this study, the weighting coefficients are treated as fixed hyperparameters. Their values are determined through preliminary trial-and-error tests to ensure stable convergence of the training process. Once selected, the same weightings are kept fixed for all experiments within given case to

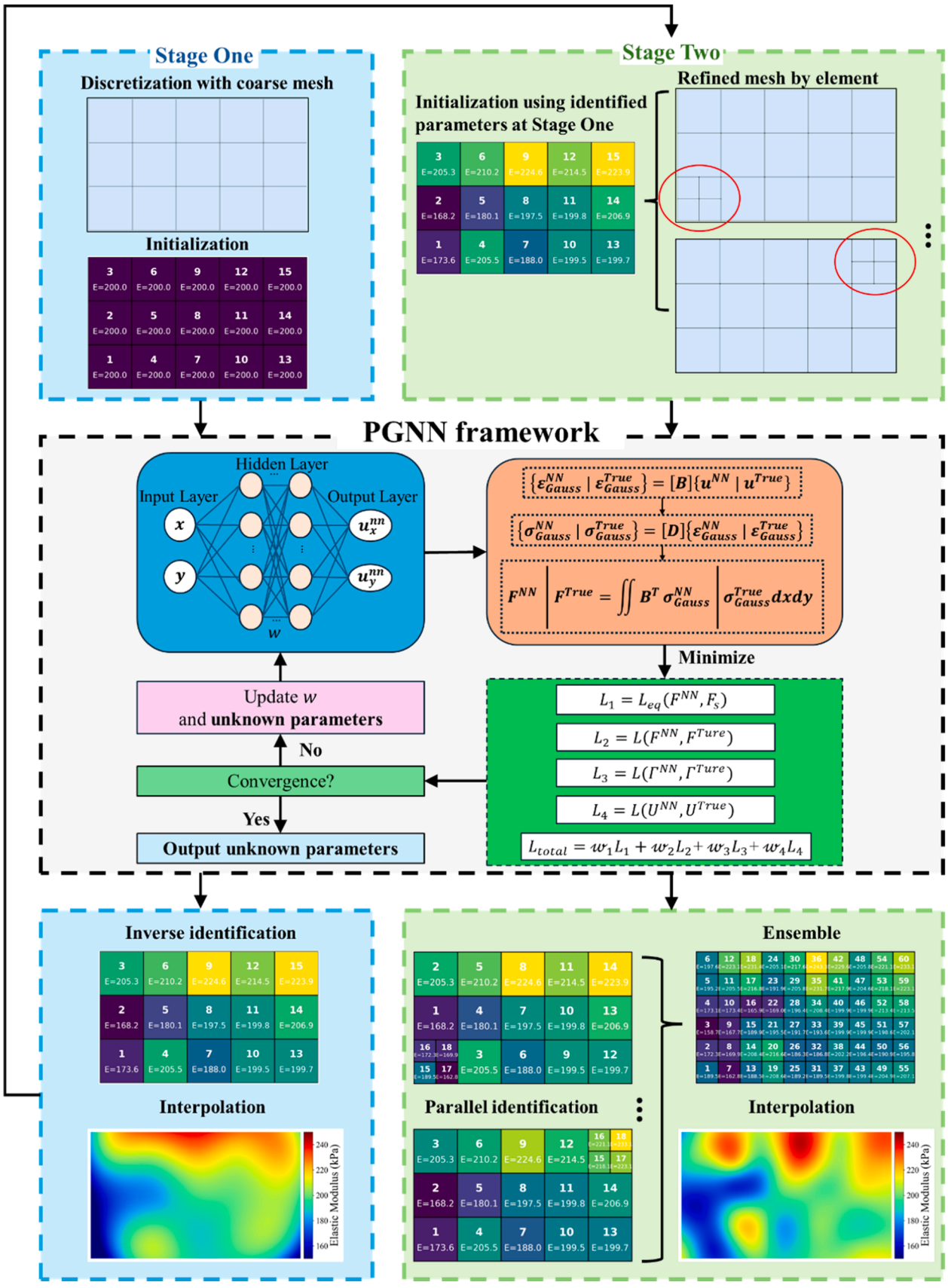


**Fig. 1.** Hierarchical physics guided neural network (HPGNN).

maintain fairness and reproducibility. In fact, there are numerous adaptive weighting coefficients design strategies for PINN, with the strategies for tuning weights vary significantly among approaches [90–93]. Our main idea is to assign relatively large weighting coefficients to amplify the effective gradients during training firstly and then adjust based on the displacement–force relationship prescribed by the constitutive model.

In practical engineering applications, $u^{True}$ represents the nodal displacement measurements, which can be obtained from instruments such as GPS stations, laser displacement transducers, settlement gauges, or distributed fiber-optic sensing systems. Similarly, $F^{True}$ corresponds to the foundation reactions or contact pressures at these nodes, which can be recorded using load cells, earth-pressure cells, or contact-pressure sensors. In the proposed framework, the nodes of the FEM discretization serve as the potential locations where such field instruments would be installed. Since field data are unavailable, these quantities are generated by a high-fidelity FEM simulation and used as ground truth for validation. As illustrated in Fig. 1, the mesh used in stage one is intentionally coarse, resulting in only a limited number of nodal points. In stage two, as mentioned above, the refinement procedure is conducted iteratively. Only introduces one additional observation point in stage two, which is subsequently moved across the domain. Consequently, the total number of measurement locations required remains limited and aligns with what can be reasonably obtained in geotechnical field monitoring.

The procedure of HPGNN can be summarized in Algorithm 1:

In addition, since extremely high precision calculations are required in this framework, a restart mechanism is incorporated to prevent the LBFGS optimizer from becoming trapped in local minima during optimization. Rao and Wang used a restarted L-BFGS algorithm in seismic waveform tomography with shot-encoding, demonstrating its high precision and stable convergence and effectively suppressing crosstalk noise [94]. Meanwhile, Byrd et al. proposed a stochastic quasi-Newton method for solving large-scale learning problems, which improves stability and convergence efficiency in stochastic environments by periodically computing sub-sampled Hessian-vector products [95]. It should be noted that the LBFGS restart mechanism is adopted as a practical engineering strategy to enhance convergence robustness and efficiency, and no novelty is claimed for the optimization algorithm itself. The restart mechanism of the LBFGS optimizer in this framework is partially adapted from the aforementioned approach and operates as follows: the optimizer periodically restarts are performed every 'A' epoch (restart interval), but only during the initial 'B' epochs (restart window). Each restart resets the optimizer state and reinitializes the trainable parameters by introducing a small random perturbation to the initial values. This mechanism can improve the computational efficiency of the HPGNN framework, and its performance will be compared with computations without the restart mechanism in the discussion section. The LBFGS Optimizer Restart Mechanism used to train HPGNN is shown in Algorithm 2:

### 2.2. Karhunen–Loève expansion random field

The heterogeneous material properties are modelled using the Karhunen–Loève Expansion (KLE). The random variable $X$ defined on a probability space $(\Xi, \Sigma, \mathrm{P})$ is a map of random events $\theta \in \Xi$ to real values in $\mathbb{R}^d$. A random process is a collection of random variables $\{X(x) : x \in \mathbb{R}^d\}$, where $x$ is an index that can typically denotes time or space [96]. In this study, the material random field is modeled as a spatial random process, corresponding to the latter case. Specifically, the random field can be viewed as a function $H(x, \theta) : \Omega \times \Xi \to \mathbb{R}$, where $x \in \Omega$ denotes a spatial coordinate in the physical domain $\Omega$ and $\theta \in \Xi$ represent a random outcome in the sample space. In addition, this work is based on a stationary Gaussian random process, and its statistical characteristics can be described by the mean function μ and the covariance function $C_{HH}(x, x')$ in Eq. (4) [97]:

$$\begin{aligned} &\mu_H(x) = \mathbb{E}[H(x,\ \theta)], \\ &\boldsymbol{C}_{HH}(\boldsymbol{x}, \boldsymbol{x}') = \mathbb{E}[\boldsymbol{H}(\boldsymbol{x},\ \boldsymbol{\theta}) - \boldsymbol{\mu}_H(\boldsymbol{x})] \cdot (\boldsymbol{H}(\boldsymbol{x}',\ \boldsymbol{\theta}) - \boldsymbol{\mu}_H(\boldsymbol{x}'))]. \end{aligned} \tag{4}$$

The covariance function is given by the Mate´rn covariance model, expressed below:

$$C_\nu(d) = \sigma^2 \frac{2^{1-\nu}}{\Gamma\nu} \left(\sqrt{2\nu}\ \frac{d}{l}\right)^{\nu} K_\nu \left(\sqrt{2\nu}\ \frac{d}{l}\right), \tag{5}$$

**Algorithm 1**
Hierarchical physics-guided neural network.

**Stage One**
1: Given the boundary conditions of the target domain, load conditions, and neural network parameters.
2: Discrete target domains with coarse mesh.
3: Initialize weights ($\boldsymbol{W}$) of the *NN* and initialization of material properties.
4: Input the nodal coordinates ($x$, $y$) into the *NN*.
5: For $i$ in range (epoch):
Output the predicted nodal displacement $\{u^{NN}\} = DNN(x, y|\boldsymbol{W})$,
Calculate the gross Gauss point strain $\{\varepsilon_G^{NN}\} = [\boldsymbol{B}]\{u^{NN}\}$,
Calculate the gross Gauss point stress $\{\sigma_G^{NN}\} = [\boldsymbol{D}]\{\varepsilon_G^{NN}\}$,
Calculate the nodal force $F^{NN} = \iint \boldsymbol{B}^T \sigma_G^{NN} dxdy$,
Calculate the loss function $\mathscr{L}$,
Back propagation and update $\boldsymbol{W}$ and material properties.
Stop if satisfy the convergence criteria.
6: Output material properties.

**Stage Two**
1: Given the boundary conditions of the target domain, load conditions, and neural network parameters.
2: Based on the coarse mesh obtained in Stage One, select one coarse element for further refinement while keeping the remaining elements unchanged.
3: Initialize weights ($\boldsymbol{W}$) of the *NN* and assign material properties using the outputs from Stage One as initial values, only set the material parameters of the refined elements as trainable while keeping other elements fixed during training.
4: Input the nodal coordinates ($x$, $y$) into the *NN*.
5: For $i$ in range (epoch):
Output the predicted nodal displacement $\{u^{NN}\} = DNN(x, y|\boldsymbol{W})$,
Calculate the gross Gauss point strain $\{\varepsilon_G^{NN}\} = [\boldsymbol{B}]\{u^{NN}\}$,
Calculate the gross Gauss point stress $\{\sigma_G^{NN}\} = [\boldsymbol{D}]\{\varepsilon_G^{NN}\}$,
Calculate the nodal force $F^{NN} = \iint \boldsymbol{B}^T \sigma_G^{NN} dxdy$,
Calculate the loss function $\mathscr{L}$,
Back propagation and update $\boldsymbol{W}$ and material properties.
Stop if satisfy the convergence criteria.
6: Output refined material properties.

**Algorithm 2**
LBFGS optimizer restart mechanism.

**Set**
1: Restart interval A.
2: Restart window B.
3: Perturbation magnitude (5 % of data noise level).
4: For $i$ in range (epoch):
1. If $i \leq B$ and $imodA = 0$:
(a) Reset LBFGS optimizer state.
(b) Apply random perturbation to trainable parameters:
$\theta = \theta + 0.05 \cdot randn(\theta)$,
*Where* $\theta$ *denotes the trainable parameters initialized from Stage One.*
2. Perform standard LBFGS optimization step.
End

where $\Gamma$ is the gamma function, $K_\nu$ denotes the modified Bessel function of the second kind, $\ell$ represents the correlation length, and $\nu$ is the smoothness parameter. For an extremely smooth random field, taking the limit $\nu \to \infty$ yields the squared-exponential covariance function:

$$\boldsymbol{C}_{+\infty}(\boldsymbol{d}) = \boldsymbol{\sigma}^2 \cdot \exp\left(-\frac{\boldsymbol{d}^2}{2l^2}\right), \tag{6}$$

where $\sigma$ is the variance, $d$ represents the distance between two spatial locations. Since random fields are essentially infinite-dimensional random processes, they are challenging to handle directly in numerical computations. The KLE is employed in this work to reduce their dimensionality into a finite set of eigenvalues $\lambda$ and eigenfunctions $f$ of the covariance operator. It is frequently involved in modelling random fields [96,98–100]. According to Mercer's theorem, the autocovariance kernel can be expressed as below [97]:

$$\boldsymbol{C}_{HH}(\boldsymbol{x}, \boldsymbol{x}') = \sum_{n=1}^{\infty} \lambda_n \boldsymbol{f}_n(\boldsymbol{x}) \boldsymbol{f}_n(\boldsymbol{x}'). \tag{7}$$

The eigenfunctions $f_n(x)$ form an orthonormal basis in the Hilbert space $L^2(\Omega)$, satisfying orthogonal normalization:

$$\int_{\Omega} \boldsymbol{f}_n(\boldsymbol{x}) \boldsymbol{f}_m(\boldsymbol{x}) d\boldsymbol{x} = \delta_{nm}. \tag{8}$$

The eigenvalues $\lambda_n$ and eigenfunctions $f_n$ are given by the following Fredholm integral equation as follows [99]:

$$\int_{\Omega} \boldsymbol{C}_{HH}(\boldsymbol{x}, \boldsymbol{x}') \boldsymbol{f}(\boldsymbol{x}') d\boldsymbol{x}' = \lambda \boldsymbol{f}_n(\boldsymbol{x}). \tag{9}$$

The random field can then be represented as an infinite sum of these eigenmodes. However, for practical computation, the series is truncated to the first $M$ dominant modes that capture most of the variance. The truncation level $M$ is typically determined by the cumulative explained variance criterion:

$$\frac{\sum_{n=1}^{M} \lambda_n}{\sum_{n=1}^{\infty} \lambda_n} \geq \eta, \tag{10}$$

where $\eta$ is usually chosen to be 95 % or 99 %. After truncation, the random field can be approximately represented as:

$$\boldsymbol{H}(\boldsymbol{x}, \boldsymbol{\theta}) \approx \widehat{\boldsymbol{H}}(\boldsymbol{x}, \boldsymbol{\theta}) = \boldsymbol{\mu} + \sum_{n=1}^{M} \sqrt{\lambda_n} \boldsymbol{f}_n(\boldsymbol{x}) \boldsymbol{\xi}_n(\boldsymbol{\theta}), \tag{11}$$

where the random variables $\xi_n(\theta)$ are a set of mutually uncorrelated random variables. They are typically assumed to follow independent standard normal variables when the random field is Gaussian ($\mathbb{E}[\xi_i] = 0$ *and* $\mathbb{E}[\xi_i \xi_i] = \delta_{ij}$).

## 3. Numerical experiment

To ensure fairness, all simulations are performed on a desktop computer with an NVIDIA RTX4090 GPU. The residual neural network (ResNet) is adopted as the backbone of the HPGNN framework, as its residual connections can effectively alleviate the vanishing gradient problem and accelerate the training process [101]. For both stage one and stage two, identical parameter configurations are used, except for the initialization and LBFGS restart strategy. Based on extensive trial-and-error experiments, the number of blocks, the number of fully connected layers, and the number of neurons per layer are set to 4, 50, and 100, respectively. A normalization layer is employed to scale the input domain to the range of [−1, 1]. The LBFGS optimizer is applied with a learning rate of 1, a gradient tolerance of 1E-30, and a loss change tolerance of 1E-32, ensuring highly precise gradient computations. For clarity, the neural network architecture and training hyperparameters are summarized in Table 9 in Appendix B. The weight of the loss function in each case is determined through repeated trial-and-error testing. The activation function is set to 'tanh' and the parameters are initialized using the 'Kaiming normal' initialization. Additionally, the neural architecture search (NAS) method proposed by Guo et al. provides a systematic approach for optimal hyperparameter selection [102]. The default loss function is the mean squared error (MSE). To guarantee high computational accuracy in inverse problems with multiple domain-wise material parameters, convergence is defined as the average change in domain material parameters remaining below a prescribed tolerance over 200 consecutive epochs, as expressed in Eq. (12).

$$\begin{aligned} &\Delta M_{avg} = \frac{1}{k} \sum_{i=1}^{k} \left| M_i^{n+1} - M_i^{n} \right|, \\ &\Delta M_{avg} < \varphi, \\ &\textbf{\textit{if}}\ \Delta \boldsymbol{M}_{avg} < \boldsymbol{\varphi}\ \textbf{\textit{for}}\ 200\ \textbf{\textit{consecutive epochs}}, \textbf{\textit{then training is terminated}}. \end{aligned} \tag{12}$$

where $M_i^n$ denotes the domain material parameters of the $i^{th}$ domain at epoch $n$, $k$ is the number of domains, and $\varphi$ is the prescribed tolerance. The value of $\varphi$ is adjusted for each case depending on the unknown parameters involved and will be specified in the corresponding sections. To evaluate the accuracy of the identified parameters, the predicted results are interpolated back onto the original fine mesh and compared against the ground truth. The overall accuracy of the reconstructed material field is quantified using the mean absolute percentage error (*MAPE*).

### 3.1. Elastic footing

To verify the effectiveness of the HPGNN framework, a two-dimensional flexible footing case study is carried out. The problem involves a weightless strip footing with a length of 20 m and a height of 12 m, subjected to a uniformly distributed downwards loading of 10 kN/m applied at the centre of the top boundary, as illustrated in Fig. 2(a). The domain is discretized using the 'Q4' element with a mesh size of 0.4, as illustrated in Fig. 2(b). The soil elastic modulus is assumed to vary spatially across elements, represented by a random field to capture material heterogeneity. Based on the KLE, the mean elastic modulus is set to 200 kPa with a coefficient of variation (COV) of 0.1, while Poisson's ratio is fixed at 0.3 throughout the domain. A Gaussian covariance function is adopted with a correlation length of 2 m and an energy threshold of 95 %. To evaluate the generalizability of the framework under different realizations of material variability, four random field realizations of the elastic modulus field are generated under identical statistical conditions, representing distinct outcomes of the same random process, as shown in Fig. 2(c) - (f). Here, a radial basis function (RBF) interpolation with a cubic kernel is employed to interpolate the discrete material parameters defined at element centers over the entire

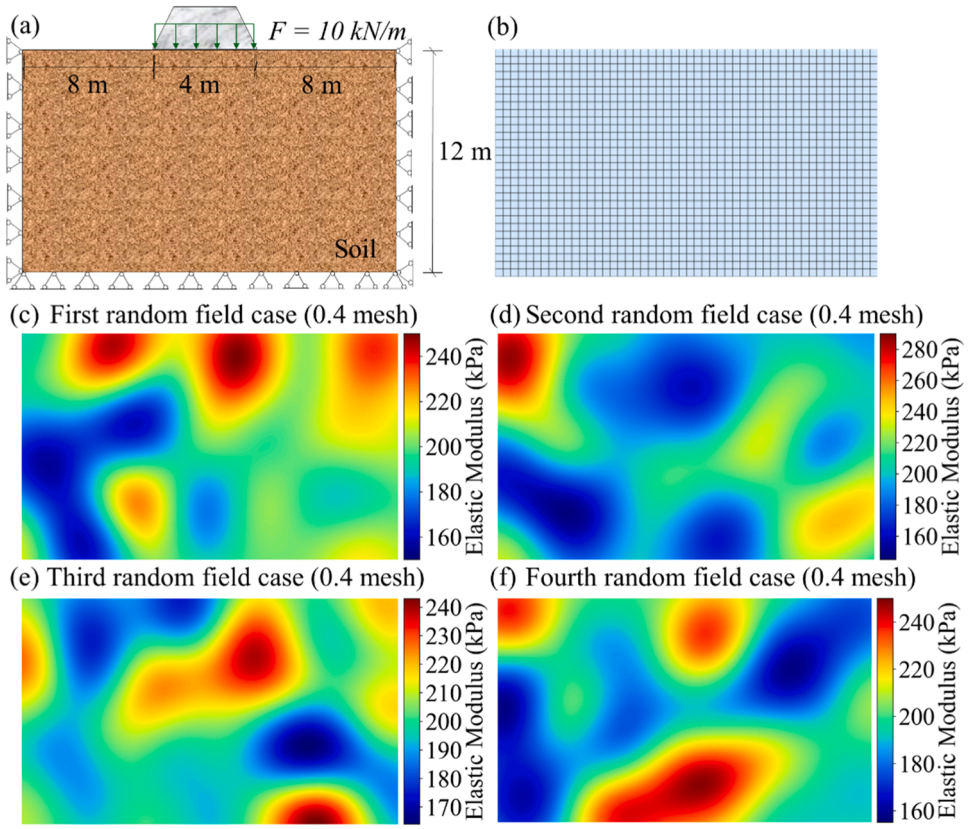


**Fig. 2.** Flexible footing (a) geometry; (b) Q4 Mesh with size 0.4; (c) - (f) four random field realizations of the heterogeneous elastic modulus.

domain. The detail is illustrated in Appendix A. These simulations allow assessment of the framework's robustness under varying spatial distributions of material properties. A hard boundary layer is imposed to enforce zero displacement at the domain boundary, ensuring precise satisfaction of boundary conditions. The initial elastic modulus for each coarse element in stage one is set to 200 kPa, with a convergence tolerance of 0.01 kPa. Through trial-and-error tests, the restart interval and restart window are chosen as 100 and 200, respectively, for stage one; in stage two, both are set to 100 epochs, and the perturbation magnitude is defined as 5 % of the data noise level. The weights of loss are set differently for the two stages. In stage one, the weighting coefficients are chosen $w_1 = 1E8$, $w_2 = 1E15$, $w_3 = 1E8$, and $w_4 = 1E11$ and with $w_1 = 1E8$, $w_2 = 1E15$, $w_3 = 1E6$, and $w_4 = 1E11$ for stage two, determined through trial-and-error tests.

In stage one of the hierarchical inverse identification process within the HPGNN framework, the entire domain is discretized using a coarse mesh of Q4 elements, as illustrated in Fig. 3(a). At this stage, only very sparse observation points are available, corresponding to the discrete locations shown in the figure, and the material parameters are identified at the coarse-element level. In stage two, each coarse element from stage one is locally refined into smaller elements, as depicted in Fig. 3(b). During this process, additional observation points are introduced within the refined region, while the remaining coarse regions remain unchanged, allowing for progressively finer-scale identification of material properties. Repeating this procedure for all coarse regions results in a fully refined domain, as presented in Fig. 3(c).

Figs. 4 and 5 illustrate the training loss and the results of four random field simulations obtained during stage one inverse analysis of the flexible footing. These results demonstrate that the HPGNN framework achieves efficient and accurate inversion of the elastic modulus across all coarse mesh elements in four random field cases, even when relying only on sparse observation data. By exploiting physics-guided constraints, the framework successfully extracts reliable material properties from limited measurements, which highlights its robustness under sparse-data conditions. Notably, the stage one inverse analysis converges within an average of 515 epochs, further demonstrating the excellent computational efficiency of the HPGNN framework.

Furthermore, the inversely identified elastic modulus values for the coarse mesh elements are presented in Fig. 5(a) below and Fig. 21(a), (c), (e) in Appendix C. Remarkably, even though only sparse observational points are employed, the proposed framework is able to recover the representative material parameters for each coarse-scale domain.

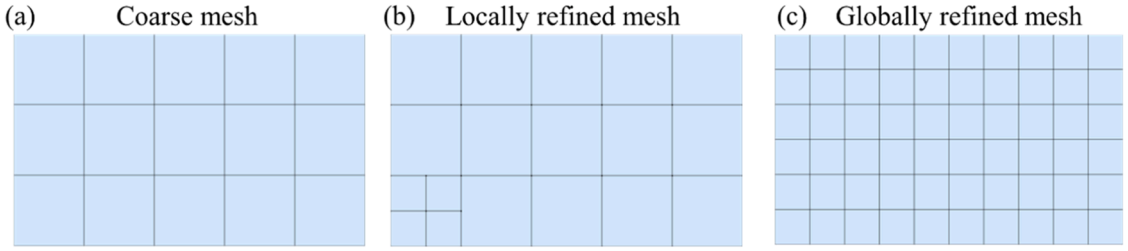


**Fig. 3.** Different meshes of flexible footing (a) coarse mesh; (b) locally refined mesh; (c) globally refined mesh.

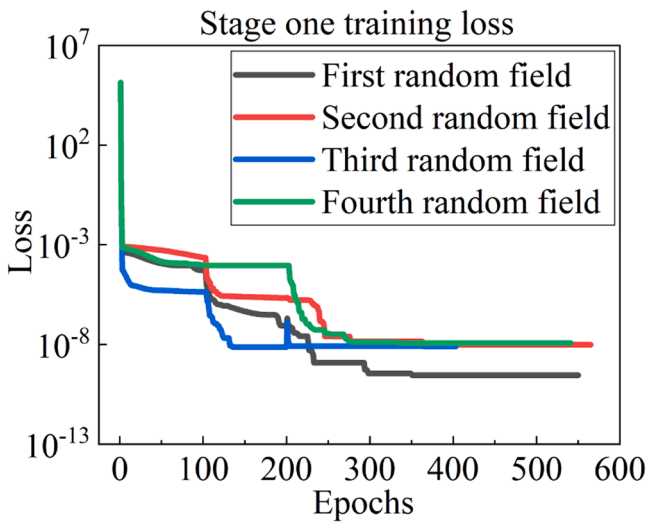


**Fig. 4.** Training loss of stage one of different random field case.

When these inversely identified coarse-scale elastic moduli are interpolated back to the original fine mesh resolution, as shown in right column of Fig. 5 below and Fig. 21 in Appendix C, the reconstructed elastic modulus fields closely resemble the ground truth random field distributions, with the MAPE remaining below 10 % across all realizations, as summarized in Table 1. By comparing Fig. 2(c) - (f) with Fig. 5(b) and Fig. 21(b), (d), (f) in Appendix C, where the color scales have been normalized for direct comparison, it is evident that the inversion based on sparse data can still capture essential spatial heterogeneity, particularly the critical zones with distinctly high or low elastic moduli.

In stage two, the coarse elements obtained from stage one is further refined, enabling the targeted selection of key regions for improved resolution. Although multiple elements could in principle be refined in parallel, a sequential strategy is adopted in this study due to computational limitations. The corresponding results are summarized in Fig. 21 in Appendix C, Fig. 6 and Table 2. During this stage, additional sparse observational data are incorporated within each coarse region, and the refinement is carried out domain by domain. This enrichment of sparse data within localized domains leads to an improvement in accuracy. As the refined coarse elements are trained individually, their loss curves are not presented separately. As shown in Figs. 6 and 21 in Appendix C, stage two of the HPGNN framework substantially enhances the representation of the random material field compared with stage one. When the resulting refined elastic modulus distributions are interpolated back to the original fine mesh resolution, the reconstructed fields closely match the reference distributions in Fig. 2(c) - (f), demonstrating a high level of fidelity. Moreover, as summarized in Table 2, the MAPE is reduced to below 2 % across all random field realizations. The average number of epochs required for each refinement is less than 500, highlighting the excellent computational efficiency. These results confirm that by sequentially introducing additional sparse data within each coarse region, the hierarchical refinement strategy can accurately recover the spatial variability of heterogeneous random fields.

To further assess the convergence behavior and inversion accuracy of the HPGNN framework, Figs. 7, 22 and 23 in Appendix C summarize the results across four random field cases. As shown in Figs. 7(a) and 22(a), (c), (e) in Appendix C, the elastic modulus of each coarse element undergoes rapid adjustments within the first two hundred epochs of stage one due to the LBFGS optimizer restart mechanism and subsequently converges. These results indicate that the framework can effectively capture the global spatial pattern of material properties at the coarse scale. To address the limited precision in coarse scale inversion, stage two performs local refinement by adding sparse data within selected coarse regions. As shown in Figs. 7(b) and 22(b), (d), (f) in Appendix C, the selected coarse element is locally subdivided into four finer elements and highlighted, while the remaining coarse elements are displayed as light curves. For clarity, only the refinement process of element one is presented. The refined elements exhibit sharp corrections within the first one hundred epochs, further validating the role of the LBFGS restart mechanism in accelerating convergence.

The absolute error of stage one results and stage two results are summarized in Figs. 7(c) - (d) and 23(a) - (f) in Appendix C. Since stage one relies on a coarse mesh, the available information for reconstructing the fine scale heterogeneous field is limited. Consequently, the interpolation results produce larger deviations, up to approximately ± 80 kPa in some regions. In contrast, the stage two results show substantially reduced error magnitudes. After performing local refinement in the target region, the inversion becomes more constrained, enabling a more accurate reconstruction of the material field. The resulting error distribution becomes more localized. This demonstrates that the stage two refinement effectively improves the ability of the framework to capture fine scale spatial variations. It is important to note that these absolute error plots represent the absolute error in kPa, and the color contrast is magnified due to the symmetric colormap scaled to the maximum absolute error. To more accurately assess accuracy, Figs. 7(e) and 23(g) - (i) in Appendix C further illustrate the element-wise APE distributions compared with the ground truth. The red bars represent stage one interpolation results, where multiple elements exhibit large errors, with some exceeding 40 %. In contrast, the blue bars correspond to stage two results, where errors are substantially reduced across all elements, with most values falling below 10 %. These results clearly demonstrate that the two-stage hierarchical refinement not only accelerates convergence but also markedly enhances the inversion fidelity of heterogeneous random fields by progressively introducing sparse data.

**Table 1**
Stage one of inversion accuracy of elastic modulus for four random field cases.

| Random field case | *MAPE of* interpolated results at original mesh size |
|---|---|
| 1 | 5.08 % |
| 2 | 5.46 % |
| 3 | 5.97 % |
| 4 | 5.29 % |

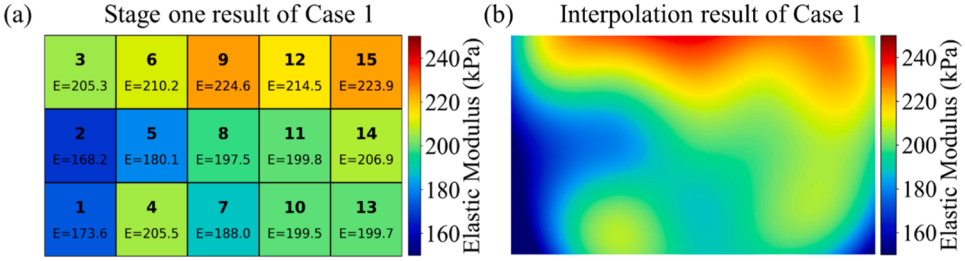


**Fig. 5.** Case one: (a) stage one inverse identification of elastic modulus for coarse meshes; (b) interpolation back to fine mesh resolution for four random filed cases.

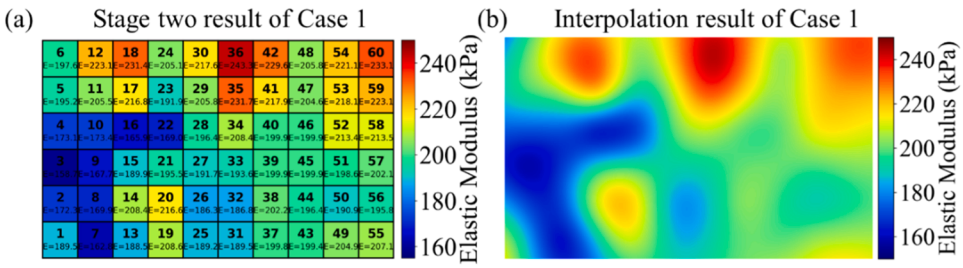


**Fig. 6.** Case one: (a) stage two inverse identification of elastic modulus for coarse meshes; (b) interpolation back to fine mesh resolution for four random field cases.

**Table 2**
Stage two inversion accuracy of elastic modulus and average training epochs per required coarse element across four random field cases.

| Random field case | MAPE *of* interpolated results at original mesh size | Average number of epochs |
|---|---|---|
| One | 1.18 % | 421 |
| Two | 1.47 % | 431 |
| Three | 1.32 % | 454 |
| Four | 1.39 % | 408 |

### 3.2. *Multiple material elastic plate*

This section evaluates the performance of the HPGNN framework in solving inverse problems involving two distinct materials. The objective is to identify the spatially varying elastic modulus fields of both materials within a plane strain plate. Owing to the inherent spatial variability and discontinuities of the material properties, this problem poses significant challenges for traditional PINNs. The problem setup is illustrated in Fig. 8(a). The boundary conditions are defined as follows: the left, right, and bottom boundaries are fully fixed, while the top is subjected to a uniformly distributed load of −2 kN/m. The elastic modulus and Poisson's ratio of the upper material (Material 1) and lower material

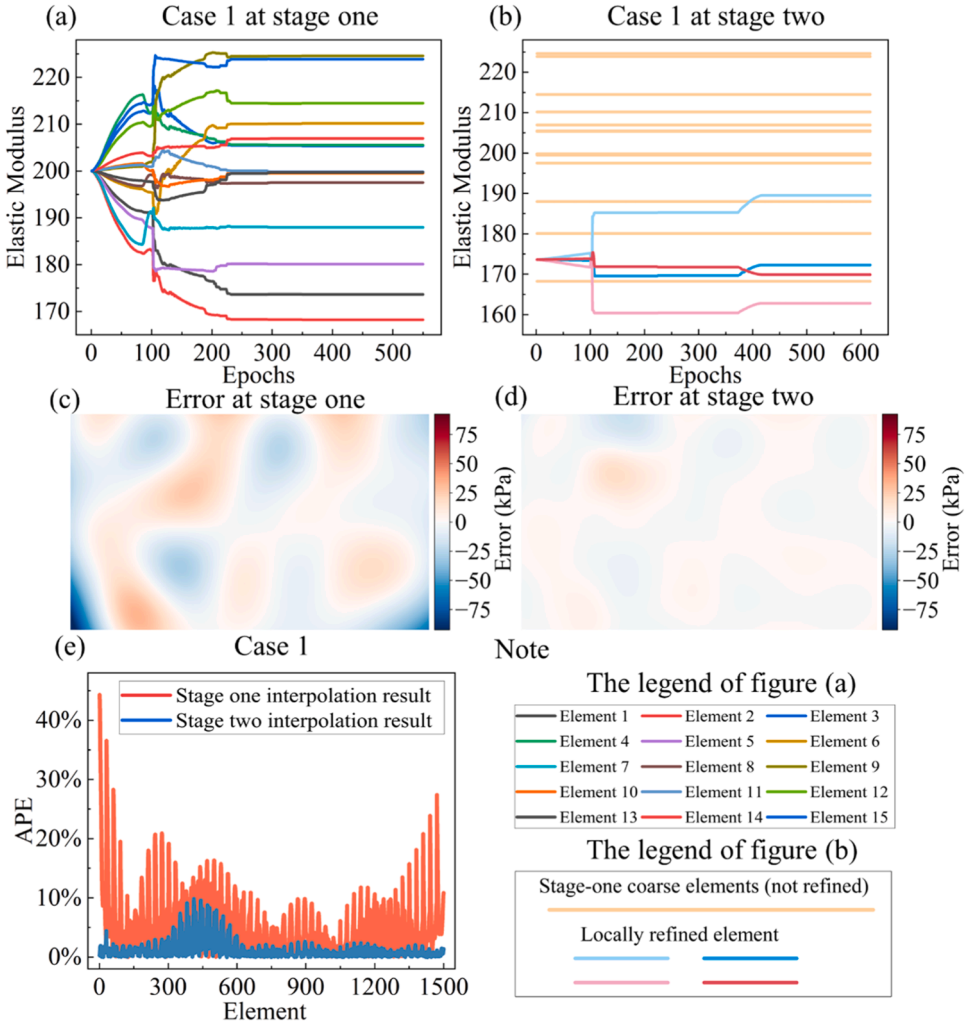


**Fig. 7.** Error analysis of the reconstructed material field: (a) convergence of element-wise elastic modulus during stage one of first random field simulations of the flexible footing; (b) convergence during stage two, where only the refinement of element 1 is shown for clarity; (c) absolute error of stage one results; (d) absolute error of stage two results; (e) element-wise absolute percentage error (APE) comparison between the two stages; note: the legend of figure (a); the legend of figure (b).

(Material 2) are set to 30 MPa and 0.4, and 50 MPa and 0.3, respectively. In this study, only the elastic modulus is modelled as a spatially varying random field. The COV for the elastic modulus of both materials is set to 0.1. A Gaussian covariance function is employed with a correlation length of 2 m, and the KLE retains 95 % of energy threshold. For the optimization settings, the restart interval and restart window are both set to 100 and 100 in stage one, and 100 and 200 in stage two, respectively, with the perturbation magnitude defined as 5 % of the data noise level. The loss function weights remain consistent between stage one and stage two, determined through trial-and-error as: $w_1 = 1E8$, $w_2 = 1E15$, $w_3 = 1E6$, and $w_4 = 1E11$. In stage one, the initial elastic modulus values for the coarse mesh are assigned as 30 MPa for elements belonging to Material 1 and 50 MPa for those in Material 2. The convergence criterion requires that both materials satisfy a tolerance of 0.01 MPa. The fine-mesh discretization of the plate is shown in Fig. 8(b). Fig. 8(c) illustrates the ground-truth random field distribution of the elastic modulus in the multi-material elastic plate, where a clear boundary is visible at the interface between the upper and lower materials. Fig. 8(d) shows the training loss during stage one, where only sparse data is employed at the coarse-mesh scale. The rapid convergence observed confirms that the HPGNN framework achieves high computational efficiency while capturing the global spatial distribution of material properties. In addition, Fig. 8 specifically illustrates the two-stage inverse identification process of the heterogeneous elastic modulus random field using the HPGNN framework, where the two material random fields are simultaneously computed. In Fig. 8(a), stage one performs a global-scale inversion on a coarse mesh to capture the dominant features of the material distribution. Based on the initial result, selected coarse elements are locally refined in stage two, as shown in Fig. 8(b) and (c), where the two material random fields are refined simultaneously. Fig. 8(d) presents the final stage-two result, revealing a high-accuracy elastic modulus field.

Fig. 9 compares the interpolated results of stage one and stage two against the ground truth shown in Fig. 8(c). As depicted in Fig. 9(a), stage one result successfully captures the overall distribution trend and identifies several anomalous regions of the modulus field. In contrast, Fig. 9(b) demonstrates that stage two refinement significantly enhances both the smoothness of the internal structure and the accuracy of the

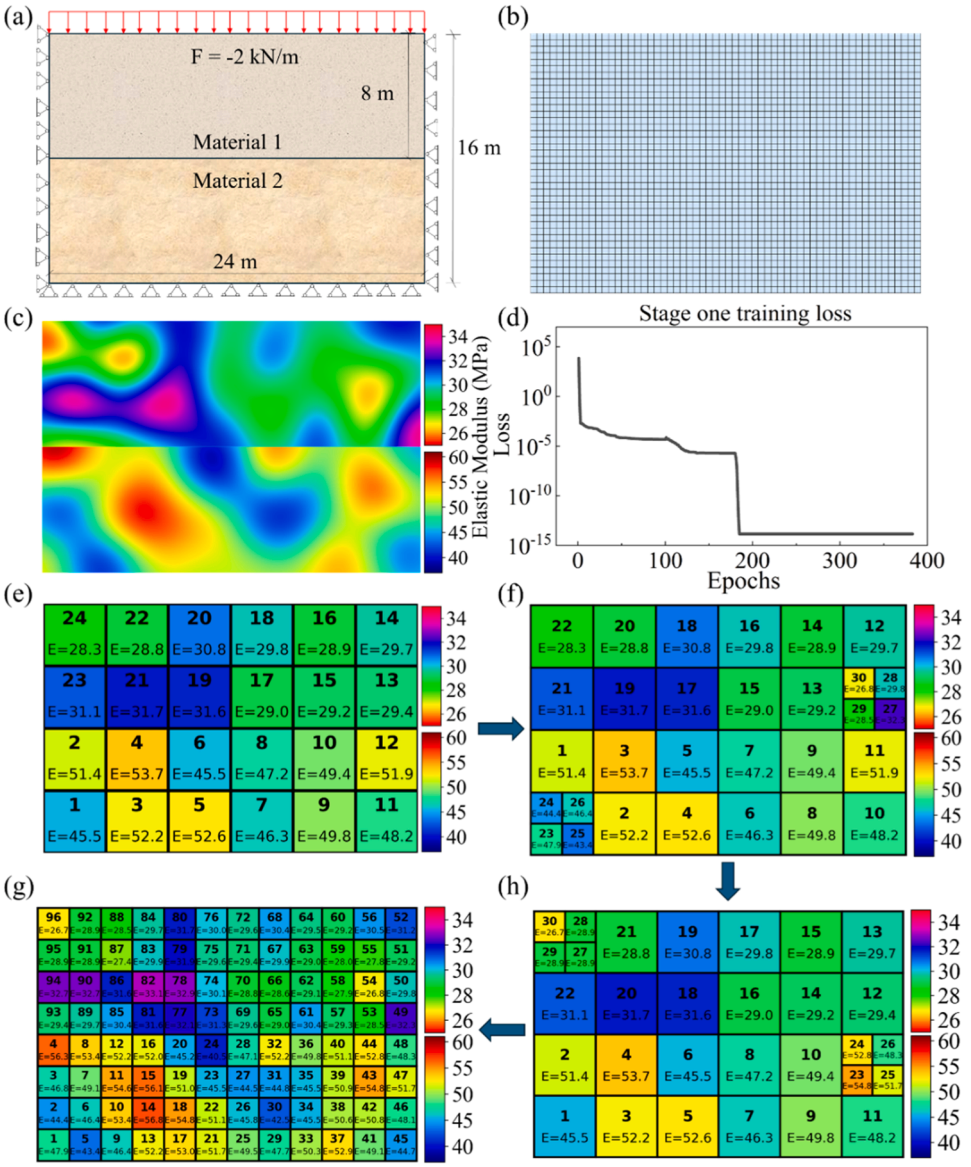


**Fig. 8.** (a) Geometry of the elastic plate; (b) finite element mesh; (c) element-wise distribution of elastic modulus; (d) training loss during stage one; two-stage inverse identification of heterogeneous elastic modulus using the HPGNN framework: (e) stage one result at the coarse scale; (f) initial refinement in stage two; (g) intermediate refinement in stage two; (h) final refined result in stage two.

prediction. This highlights the potential of the HPGNN framework in accurately resolving complex and highly heterogeneous material identification problems. Table 3 further demonstrates the high accuracy and efficiency of the HPGNN framework, with the interpolated MAPE reduced from 5.73 % in stage one to 0.88 % in stage two.

Fig. 10 illustrates the convergence of the elastic modulus throughout the two-stage training process. As shown in Fig. 10(a), during the stage one training on a coarse mesh, the model converges rapidly and captures the overall distribution trends of the elastic modulus fields for both materials. As shown in Fig. 10(b), selected elements of the two materials are locally refined, enabling a more accurate characterization of the spatial variability of the material properties. For clarity, only the refinement process of element 1 from each material is displayed, while the remaining coarse elements are kept unchanged. This targeted refinement demonstrates how the elastic modulus of selected elements progressively adjusts toward more accurate values.

As shown in Fig. 10(c) and (d), the absolute error is compared between stage one and stage two. In Fig. 10(c), the stage one produces large and spatially uneven errors, particularly in regions with transitions between the two materials. These deviations indicate that the stage one is unable to accurately capture fine scale variations within the heterogeneous domain. After refinement, the error distribution in Fig. 10(d) is improved. Most areas exhibit much smaller errors, demonstrating that the hierarchical refinement can effectively reconstruction material field. The quantitative comparison in Fig. 10(e) further reinforces this improvement. The red bars represent the element-wise APE obtained in stage one, which are noticeably high in some regions, whereas the blue bars denote stage two refinements. The stage two refinement significantly reduces the APE across all elements of the two-material random field, clearly demonstrating the effectiveness of the HPGNN framework in addressing inverse material identification problems with strong heterogeneity.

## 4. Discussion

### 4.1. Random input perturbations

To assess the robustness of the HPGNN framework with sparse observational data under different random field conditions, we perform two sets of comparisons by varying the coefficient of variation (COV) and the correlation length (CL) of the random elastic modulus fields in the multi-material elastic plate. Since the stage-two results build directly on stage one and the underlying algorithm remains essentially the same, only stage one is considered here. The corresponding results are summarized in Figs. 11-16, and Table 4.

Fig. 11 shows the spatial distribution of the elastic modulus field at different COV levels (5 %, 10 %, 15 % and 20 %), while Fig. 12 presents the results under different CLs (1 m, 2 m, 3 m, and 4 m). It can be observed that higher COV values introduce greater variability into the stochastic input, whereas larger CLs result in smoother patterns. Fig. 13 further indicates that variations in random input perturbations exert limited influence on the convergence rate, as all curves stabilize at a similar loss level within a comparable number of epochs. However, Table 4 shows that increasing the COV and decreasing the CL can lead to higher MAPE in the interpolation results. This suggests that additional refinement stages within the HPGNN framework may be required to achieve finer element meshes and improve the fit to the original random elastic modulus field. Nevertheless, even with sparse observational data, the HPGNN framework consistently demonstrates stable performance across all random input perturbations, underscoring its robustness in handling strong variability.

**Table 3**
Inversion accuracy of elastic modulus and average training epochs in stage one and stage two.

| Stage | *MAPE of* interpolated results at original mesh size | Average number of epochs |
|---|---|---|
| 1 | 5.73 % | 383 |
| 2 | 0.88 % | 507 |

### 4.2. LBFGS restart mechanism

In neural networks, a well-chosen initial guess can substantially reduce computational costs, whereas an extreme initial value may lead to prolonged convergence and a significant increase in computational burden [103,104]. Since the initial values in stage two of the HPGNN framework fully depend on the convergence results of stage one, this section investigates the impact of extreme initial guesses in stage one for both the footing and the multi-material plate problems. Specifically, for the footing case under the first random field, the initial elastic modulus is set to an extremely low value of 1 kPa, while for the plate, the initial values of both the upper and lower materials are set to 1 MPa.

Fig. 14 presents the training losses of the two cases under identical LBFGS restart parameters, comparing the performance between extreme and well-chosen initializations. The red curves correspond to the training losses under extreme initialization, while the black curves represent the results obtained with good initial values. It is evident that, under the same convergence criteria, extreme initial values exert an adverse influence on the optimization process. For the footing case, the model still manages to converge, though at a noticeably slower rate than with good initialization. By contrast, the multi-material plate case fails to converge even after reaching the maximum number of epochs, exhibiting significantly higher loss and indicating that the model is unable to accurately capture the target values.

These results indicate that extreme initialization can impair the training performance of the HPGNN framework, reflecting the inherent sensitivity of neural networks to initial conditions. To overcome this limitation, it is essential to adopt strategies that mitigate the adverse

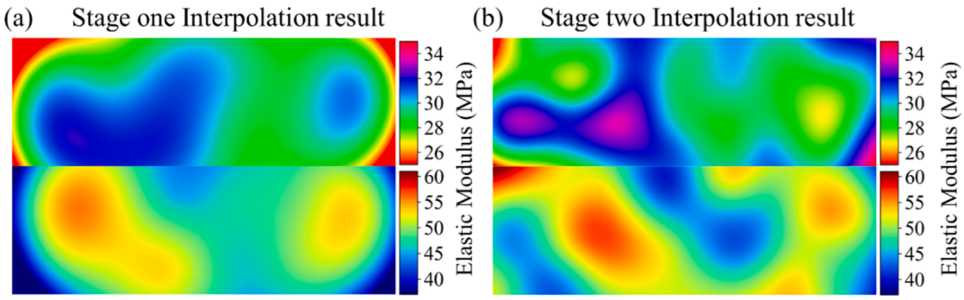


**Fig. 9.** Elastic modulus fields on the original mesh obtained by interpolation: (a) result from stage one; (b) result from stage two.

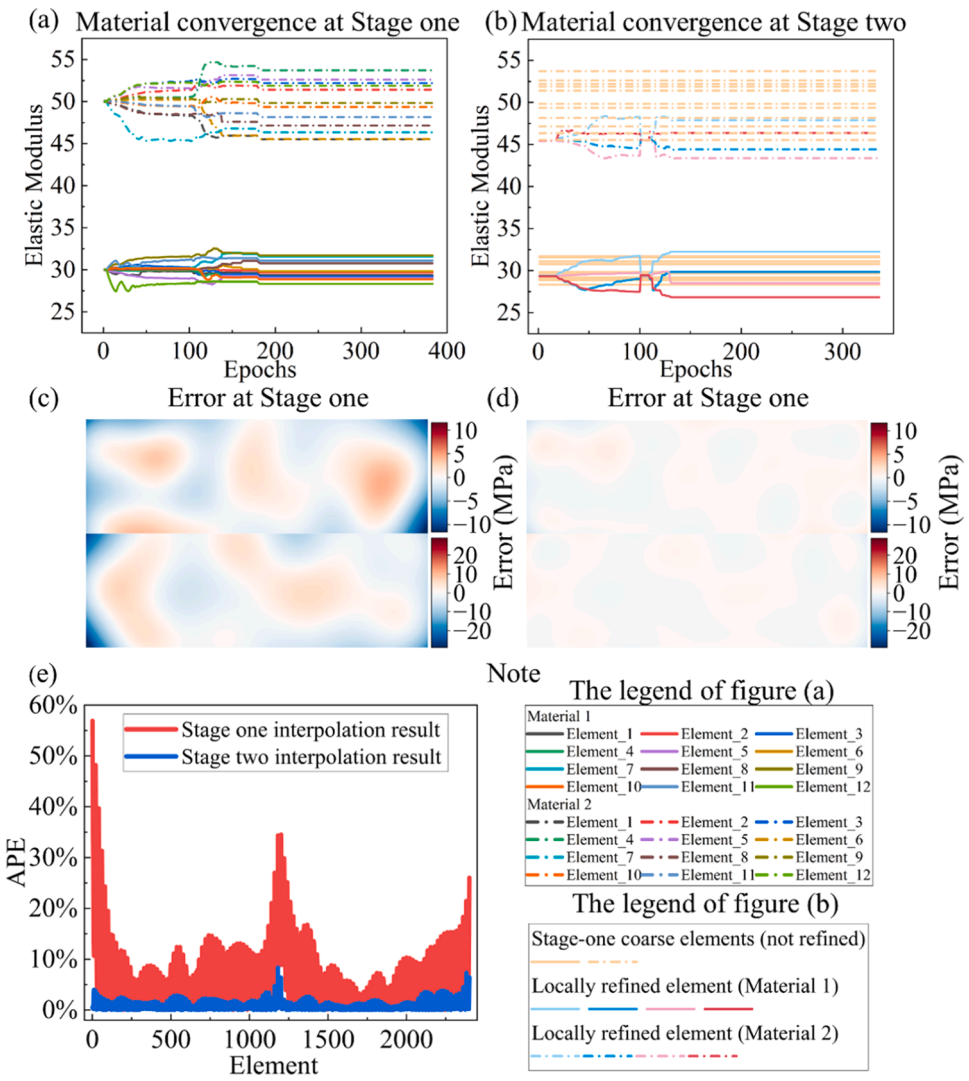


**Fig. 10.** Error analysis of the reconstructed material field: (a) convergence of elastic modulus during stage one training; (b) convergence of elastic modulus during stage two training; (c) absolute error of stage one results; (d) absolute error of stage two results; (e) element-wise absolute percentage error (APE) comparison between the two stages; note: the legend of figure (a); the legend of figure (b).

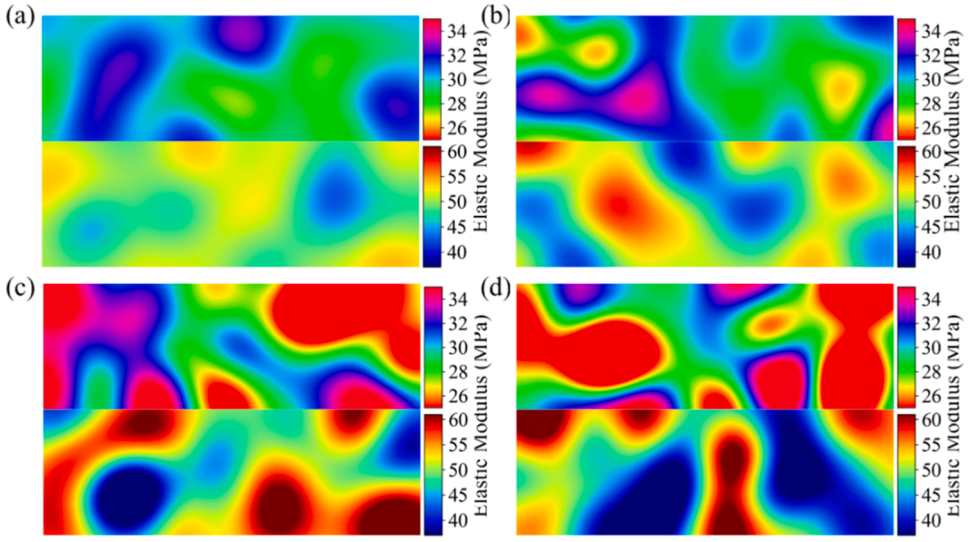


**Fig. 11.** Results of the HPGNN framework under different COVs of the random elastic modulus fields in multi-material elastic plate: (a) COV = 5 %; (b) COV = 10 %; (c) COV = 15 %; (d) COV = 20 %.

**Table 4**
Inversion accuracy and average training epochs of HPGNN framework under different KLE parameters.

| Evaluation metric | Different COVs | | | | Different CLs | | | |
|---|---|---|---|---|---|---|---|---|
| | 5 % | 10 % | 15 % | 20 % | 1 m | 2 m | 3 m | 4 m |
| *MAPE of* interpolated results at original mesh size (%) | 3.55 | 5.73 | 6.87 | 9.79 | 7.29 | 5.73 | 4.85 | 3.37 |
| Number of epochs | 371 | 383 | 493 | 398 | 377 | 383 | 418 | 403 |

effects of poor initialization. Accordingly, the remainder of this section investigates the role of the LBFGS restart mechanism in improving convergence under extreme initialization. The objective is to further demonstrate its effectiveness in stabilizing the training process, particularly when only sparse observational data are available.

The green curves in Fig. 15 correspond to the setting where both the restart window and interval are set to zero, meaning that the LBFGS restart mechanism is not applied. For both cases, convergence appears relatively smooth at the beginning, and the initial loss decreases in a manner comparable to the cases with the restart mechanism. However, as training progresses, the rate of decrease slows significantly, and the final loss remains at a high level. This indicates that the model becomes trapped in a local minimum, preventing accurate identification of the domain material properties. In contrast, the blue curves show the training losses obtained using the newly tuned LBFGS restart mechanism parameters in the ablation study. Notably, even under extreme initial conditions with sparse data, the model converges rapidly and achieves lower loss within a relatively small number of epochs. This highlights the effectiveness of the LBFGS restart mechanism in significantly enhancing the robustness and convergence efficiency of HPGNN. A comparison between Figs. 14 and 15 examines the performance of the LBFGS restart mechanism under different restart parameter settings. By appropriately tuning the restart window and interval, the framework can escape local minimum and achieve optimal training performance, even in the presence of extreme initialization and sparse data. It can be concluded that employing the LBFGS restart mechanism with properly tuned restart parameters can enhance computational efficiency by up to 90 % compared to cases without the mechanism.

Fig. 16 shows the corresponding behavior of the mean elastic modulus, demonstrating how the LBFGS restart mechanism accelerates convergence under challenging initialization conditions. In Fig. 16(a), corresponding to the first random field case of elastic footing, the target mean elastic modulus is 200 kPa, indicated by the purple dashed line.

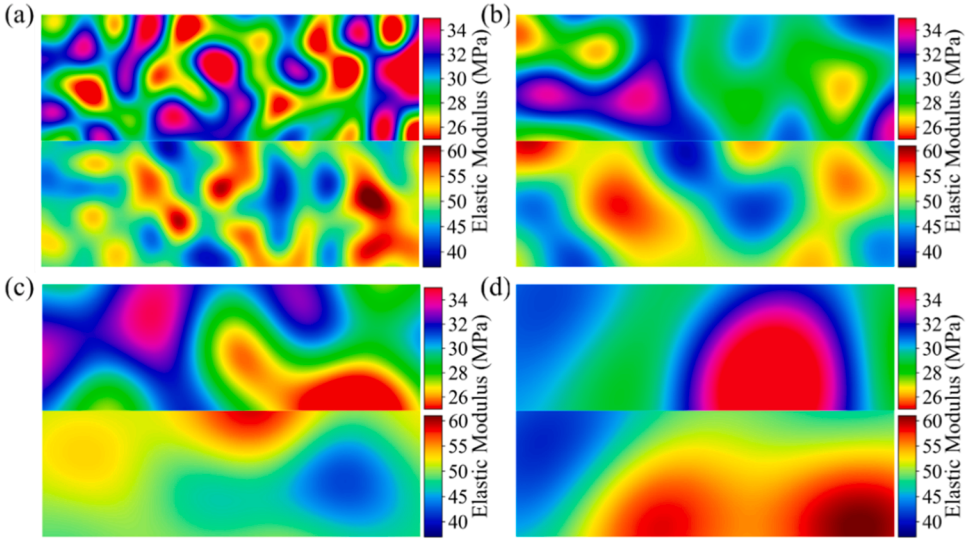


**Fig. 12.** Results of HPGNN framework under different correlation lengths (CL) of the random elastic modulus fields in multi-material elastic plate: (a) CL = 1 m; (b) CL = 2 m; (c) CL = 3 m; (d) CL = 4 m.

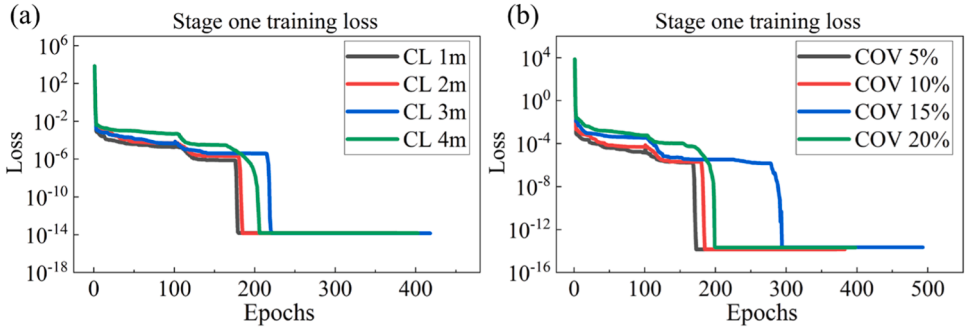


**Fig. 13.** Stage one training loss of the HPGNN framework under different KLE parameters: (a) comparison of varying coefficients of variation (COV = 5 %, 10 %, 15 %, 20 %); (b) comparison of different correlation lengths (CL = 1 m, 2 m, 3 m, 4 m).

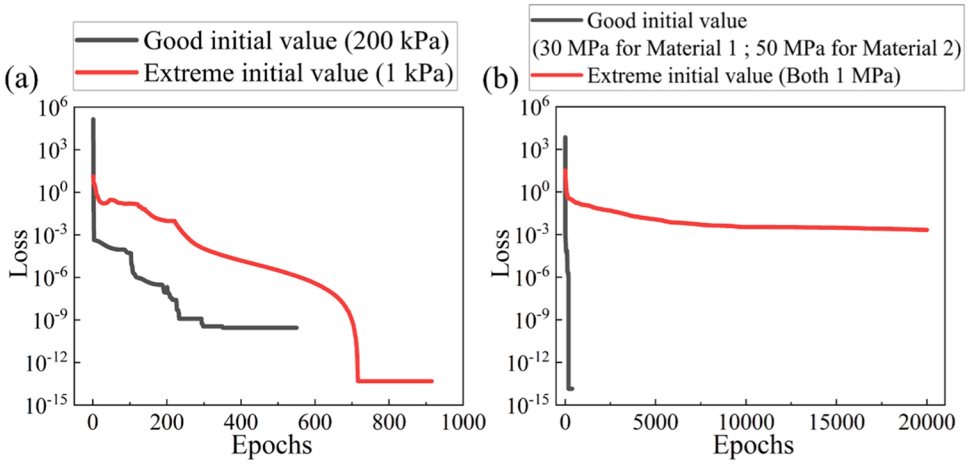


**Fig. 14.** Training loss under identical LBFGS restart parameters with extreme initialization in the HPGNN framework: (a) elastic footing; (b) multi-material elastic plate.

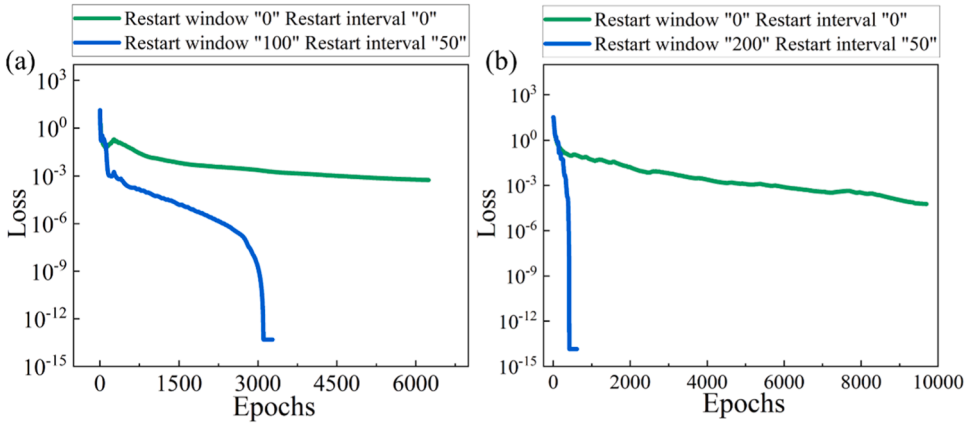


**Fig. 15.** Effect of the LBFGS restart mechanism on training loss under extreme initialization in the HPGNN framework: (a) elastic footing; (b) multi-material elastic plate.

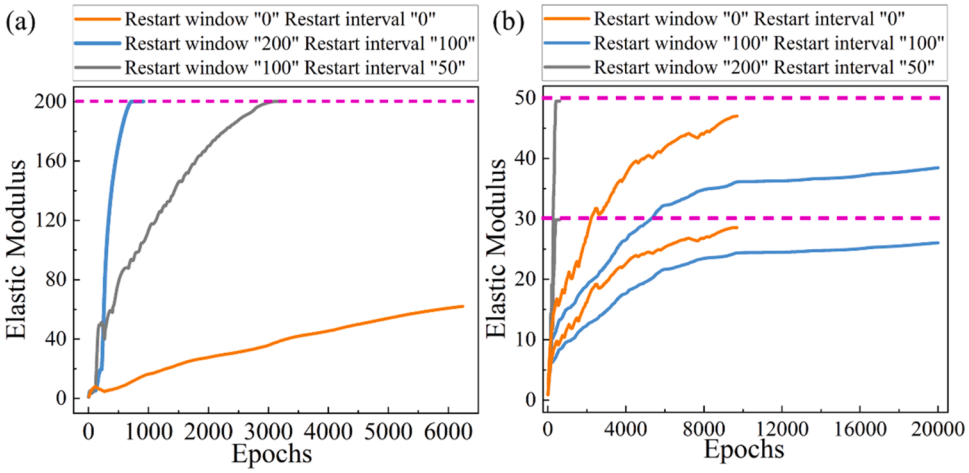


**Fig. 16.** Convergence of mean elastic modulus under different LBFGS restart mechanism parameters with extreme initialization in the HPGNN framework: (a) elastic footing; (b) multi-material elastic plate.

The orange curve clearly converges to an incorrect value, while the gray and blue curves converge rapidly and accurately to the ground truth, highlighting the effectiveness of the restart strategy. This indicates that a well-designed LBFGS restart mechanism can substantially enhance training performance. Similarly, Fig. 16(b) presents the results for the multi-material elastic plate, where the mean elastic moduli of the two materials are 30 MPa and 50 MPa, respectively, also marked by purple dashed curves. In this more complex case, the orange curve again fails to reach the correct values, and the gray curve only partially approaches the targets. In contrast, the blue curve exhibits fast and precise convergence toward both true moduli, demonstrating that properly selected restart parameters can substantially improve the robustness of the framework.

Overall, these results illustrate that while the early convergence trends of different parameters appear similar, their long-term behavior diverges significantly. The LBFGS restart mechanism enables the HPGNN framework to escape poor local minimum even under challenging initialization. Although the detailed information of the restart mechanism is beyond the scope of this study, its demonstrated effectiveness suggests promising potential for broader application to other neural network frameworks in future work.

### 4.3. Noise sensitivity

In inverse problems, ground truth data are typically used as reference solutions. Within the proposed HPGNN framework, the available observations are provided in the form of sparse labels obtained from FEM-based simulations followed by interpolation. In real-world engineering applications, such measurements are often contaminated by noise arising from sensor inaccuracies and environmental disturbances, which poses significant challenges for neural network based inverse identification. To evaluate the robustness of the proposed HPGNN framework under sparse and noisy label conditions, the first elastic footing example presented in Section 3.1 is employed. Gaussian noise with different

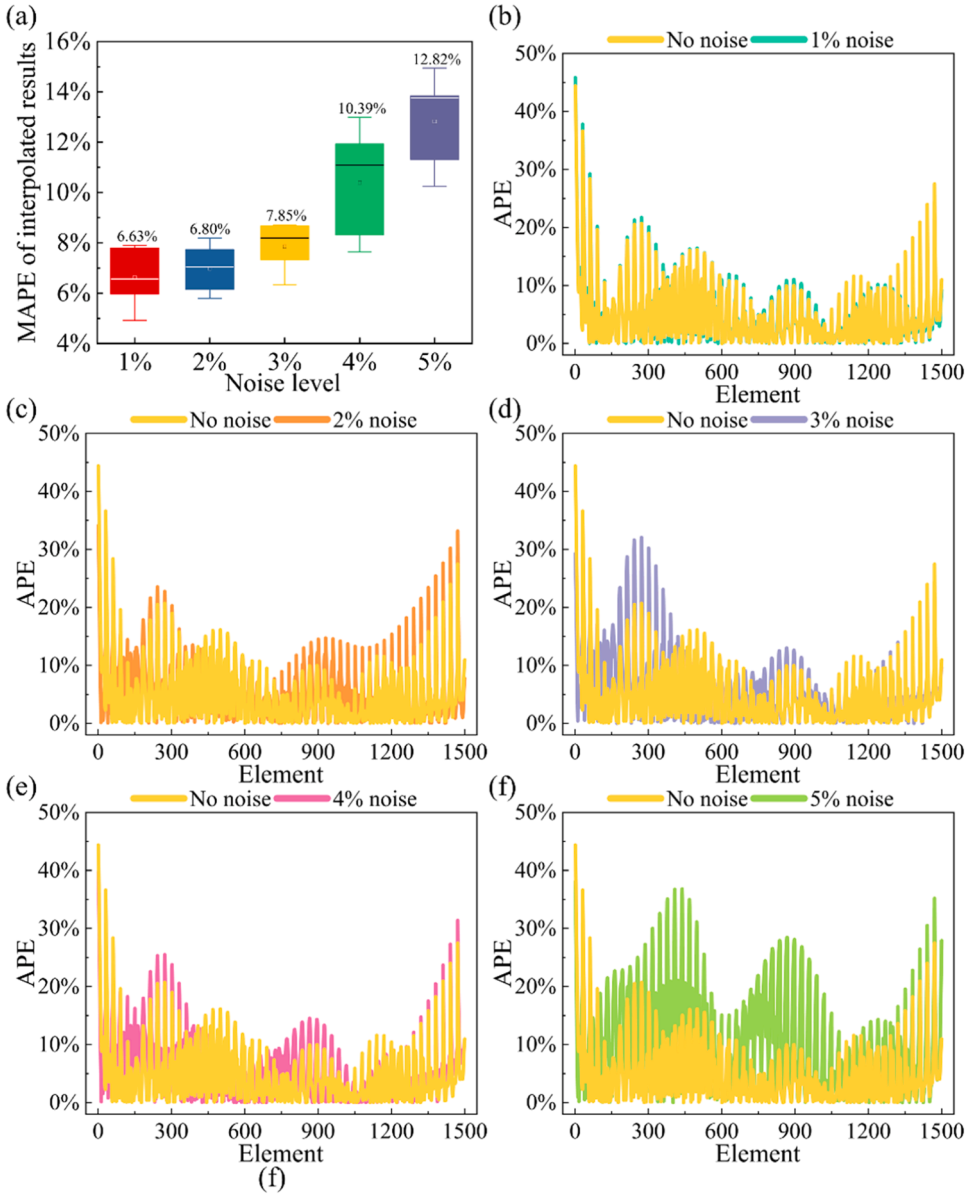


**Fig. 17.** Noise sensitivity and uncertainty analysis of the inverse identification results: (a) MAPE of the interpolated material field under different noise levels based on five independent realizations (top is mean value); (b - f) element-wise average APE distributions for noise levels of 1 %–5 % compared with the noise-free case.

intensity levels is added to the sparse labels, and for each noise level, five independent realizations are performed to quantify noise-induced uncertainty.

Fig. 17(a) presents the distribution of the MAPE of the interpolated material field across different noise levels. As the noise level increases from 1 % to 5 %, both the median MAPE and its dispersion exhibit a clear upward trend, indicating a degradation in inversion accuracy and increased variability of the results. Fig. 17(b) to (f) further illustrate the element-wise APE distributions averaged over five realizations, in comparison with the noise-free case. For 1 % to 2 % noise levels, the majority of elements exhibit error levels comparable to those of the noise-free scenario, and the reconstructed material field successfully captures the global trends. When the noise level reaches 3 %, localized fluctuations in the APE begin to emerge. At 4 % to 5 % noise levels, these fluctuations become more pronounced, with some elements showing significantly elevated errors, indicating that noise effects are amplified through sparse data. A quantitative summary of the noise impact is provided in Table 5, which reports the average MAPE of the interpolated material field at the original mesh resolution. The mean MAPE increases from 6.63 % at 1 % noise to 12.82 % at 5 % noise, with intermediate values of 6.80 %, 7.85 %, and 10.39 % for noise levels of 2 %, 3 %, and 4 %, respectively. Despite this degradation, the overall error remains below 15 % even at the 5 % noise level considered, which is generally acceptable for many geotechnical engineering inverse analyses.

These results confirm that the proposed HPGNN framework exhibits reasonable robustness to different levels of measurement noise, while also highlighting its sensitivity to noise under sparse data. Sparse labels inherently introduce errors that are further amplified in the presence of noise. The findings emphasize the importance of incorporating appropriate noise mitigation or denoising strategies to improve the accuracy of inverse identification in real-world engineering applications. Future work will focus on integrating such strategies within the HPGNN framework to further improve its robustness in practical applications.

### 4.4. Label sensitivity and hierarchical benchmark studies

#### 4.4.1. Influence of the number of label points

To investigate how the number of label points affects the quality of material property identification, four cases with 15, 20, 24, and 35 label points are evaluated for the elastic footing case under the first random field in stage one. Each label point corresponds to a node in the FEM discretization, meaning that increasing the number of label points can increase the spatial resolution of the measurement field.

Fig. 18 illustrates the four mesh configurations and their corresponding reconstruction results. When only 15 label points are used, the inverse model fails to recover the general trend of the heterogeneous field. As the number of label points increases to 20, 24, and 35, the reconstructed material fields progressively become consistent with the true distribution, indicating that additional label points can improve identifiability. The training loss curves in Fig. 18(i) show that models with more label points have lower loss values, although a higher number of epochs is required for convergence. As shown in Fig. 18(j), the boxplot clearly shows that increasing the number of label points not only reduces the median APE but also significantly suppresses error dispersion and extreme outliers. Specifically, the reconstruction suffers from large variability and severe local errors with using 15 points, whereas using 24 or more label points leads to stable identification. A quantitative summary is provided in Table 6. The MAPE reduces from 29.76 % with 15 label points to 3.65 % with 35 label points, demonstrating that increasing the label points can enhance the inversion accuracy. The training time and peak GPU memory consumption are also summarized. As the number of label points increases from 15 to 35, the training time increases accordingly due to the additional data. In contrast, the peak GPU memory usage remains nearly constant, at approximately 150 MB for all cases. This demonstrates that the memory is mainly occupied by the FEM and neural network components rather than the number of locally refined material parameters. This confirms that the hierarchical strategy effectively controls memory usage and avoids the dimensional explosion that would arise from direct fine-mesh inversion.

In summary, the accuracy improvement comes at the cost of increased computational time. In practical engineering applications, a larger number of measurement locations also implies higher instrumentation and operation costs. In this case, a balance between label points, accuracy requirements, and overall efficiency must be considered.

**Table 5**
Average MAPE of the interpolated material field under different noise levels.

| Noise | *Average MAPE of* interpolated results at original mesh size |
|---|---|
| 1 % | 6.63 % |
| 2 % | 6.80 % |
| 3 % | 7.85 % |
| 4 % | 10.39 % |
| 5 % | 12.82 % |

#### 4.4.2. Evaluation of direct inversion feasibility on fine mesh

To examine whether a conventional single-scale inversion can be performed directly on the heterogeneous material, an inverse analysis is attempted in this section using the baseline mesh size with 0.4 for the elastic footing case.

The results are summarized in Fig. 19. As shown in Fig. 19(a), although the loss decreases slightly during the initial iterations, it quickly satisfies the convergence condition. The mean parameter changes across the entire domain displayed in Fig. 19(b) shows that, except for changes caused by the LBFGS restart mechanism, the update magnitude remains extremely small throughout the entire training process. In this case, the optimization landscape becomes flat, preventing LBFGS producing effective search directions. The ground truth and reconstructed material field are shown in Fig. 19(c) and (d) respectively, further indicating that the optimizer is unable to update the heterogeneous material parameters. This failure is rooted in the high dimensionality of the fine mesh inverse problem. When hundreds of local material parameters are updated simultaneously, their individual contributions to the global response become weak. In this case, the sensitivity of the governing equations with respect to each parameter diminishes, causing the gradients to vanish. As a result, the optimizer is unable to escape the initial state, indicating that inverse identification cannot be achieved under the single-scale approach. In contrast, the proposed two-scale hierarchical strategy avoids this difficulty. By performing the inverse identification first on a coarse mesh, the model estimates only rely on a small number of parameters. Then the coarse scale results act as physically meaningful initialization for the refined stage, where the parameter space is a little larger but initialized close to the true trend. This prevents the optimizer from entering the vanishing-gradient region that happened in the direct fine mesh inversion. Through this hierarchical progression, the two-scale method can capture both global and local variations efficiently, enabling accurate reconstruction that is unattainable under a traditional single-scale inversion.

These findings demonstrate that direct inverse analysis on the fine mesh is computationally infeasible, while the proposed hierarchical two-scale framework provides a stable alternative capable of recovering high resolution heterogeneous material fields.

#### 4.4.3. Comparison with operator-learning-based methods

To further demonstrate the advantages of the proposed HPGNN framework, a direct comparison is conducted in this section with DeepONet framework, using the elastic footing under sparse data as a benchmark. In the DeepONet, an inverse operator is trained to directly map the displacement field to the heterogeneous elastic modulus field. 100 realizations of datasets ($x$, $y$, $E$, $u_x$,$u_y$) are generated at fine element

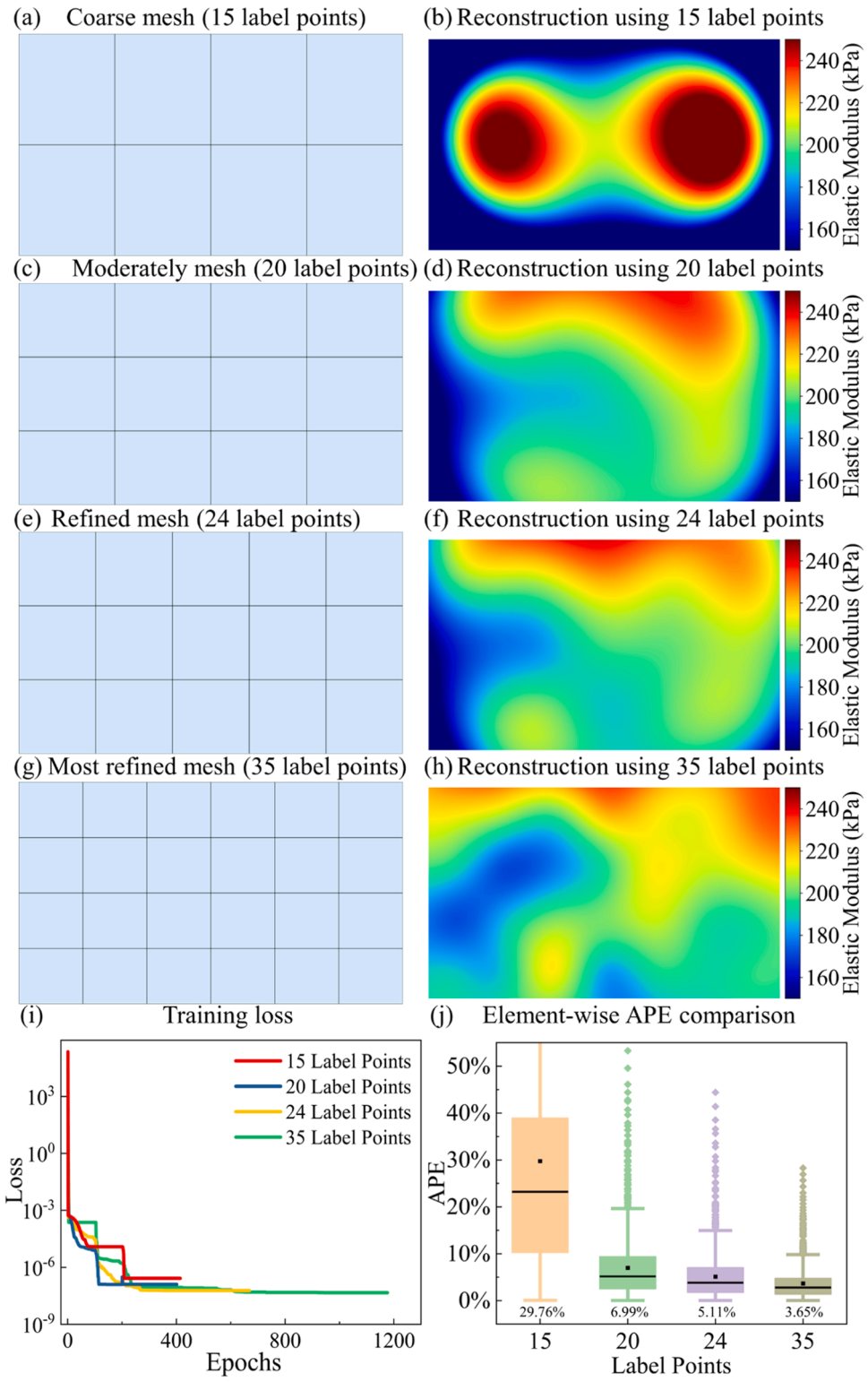


**Fig. 18.** Influence of label points density on reconstructed material fields: (a), (c), (e), (g) meshes with 15, 20, 24, and 35 label points; (b), (d), (f), (h) corresponding reconstructed material fields under each label point configuration; (i) loss for 15, 20, 24, and 35 label points; (j) element-wise APE comparison for different label point configurations (bottom is mean value).

**Table 6**
Effect of the number of label points on reconstruction accuracy and computational cost.

| The number of label points | *MAPE of* interpolated results at original mesh size | Training time (sec) | Peak GPU memory (MB) |
|---|---|---|---|
| 15 | 29.76 % | 87.14 | 149.66 |
| 20 | 6.99 % | 114.36 | 149.75 |
| 24 | 5.11 % | 182.82 | 150.48 |
| 35 | 3.65 % | 1050.56 | 150.90 |

centres using FEM. The dataset is split into 80 training cases and 20 validation cases. In the DeepONet formulation, the branch network takes the flattened displacement field ($u_x$,$u_y$) as input, while the trunk network takes the normalized spatial coordinates ($x$,$y$) as query locations. These two subnetworks are fused followed by a linear output layer to predict the elastic modulus at each element centre. The network is trained using full-batch LBFGS optimization, and once trained, the elastic modulus field can be inverse directly without any additional optimization. Table 7 summarizes the hyperparameter configuration of the DeepONet to ensure reproducibility.

To ensure a fair comparison, the trained DeepONet is evaluated on the same four random-field cases used in the HPGNN experiments. The results obtained using the DeepONet and the proposed HPGNN framework are compared in Fig. 20(a) to (l). While DeepONet can capture the overall spatial trend of the elastic modulus distribution in case 2 and case 3, noticeable local discrepancies can be observed in case 1 and case 4. This behavior is mainly attributed to the fact that DeepONet is often trained on a dataset generated from dense and high-fidelity simulation data. When applied to inverse problems with sparse measurements and limited effective samples, the data-driven inverse operator becomes unstable. In contrast, HPGNN provides more accurate reconstructions of the heterogeneous elastic modulus fields, preserving local variations more effectively. Fig. 20(m) to (p) present the element-wise APE distributions for DeepONet and HPGNN across four random-field realizations. DeepONet suffers from large local errors and significant oscillations at the element level, with peak APE values exceeding 40 % in some regions. In contrast, HPGNN consistently yields lower distributed errors, with substantially reduced peaks. The quantitative results are summarized in Table 8. For the four test cases, the MAPE of the interpolated fine-mesh results ranges from 3.61 % to 14.31 % for DeepONet, whereas HPGNN consistently achieves significantly lower errors, with MAPE values between 1.18 % and 1.47 %. These results highlight a difference between the two approaches. DeepONet learns a purely data-driven inverse operator and therefore requires a large number of training datasets, making it sensitive to data scarcity. In contrast, HPGNN embeds the inverse problem within a physics-guided framework. This strategy enables HPGNN to achieve higher accuracy and improved computational efficiency, particularly in sparse data scenarios that are common in practical inverse analysis problems.

## 5. Conclusion

In this study, we proposed a novel Hierarchical Physics-Guided Neural Network (HPGNN) framework for the inverse identification of heterogeneous material properties using sparse data labels. By integrating the interpretability of the FEM with the learning capability of neural networks, HPGNN adopts a two-stage training strategy that progressively transitions from coarse to a refined scale. Numerical experiments demonstrate that HPGNN exhibits strong robustness across various random field realizations, achieving the MAPE of the identified random field material properties consistently below 2 %. In multi-material cases, the framework further achieves an average MAPE of only 0.88 % across two distinct random material fields.

**Table 7**
Hyperparameter settings of the DeepONet.

| Category | Parameter | Value |
|---|---|---|
| Branch network | Architecture | Linear layer |
| | Hidden layers | 1 |
| | Output dimension | 128 |
| Trunk network | Hidden layers | 4 |
| | Neurons per layer | 256 |
| | Activation function | Tanh |
| | Output dimension | 128 |
| Optimizer | Optimizer type | LBFGS |
| | Learning rate | 1 |
| | Iterations | 2000 |

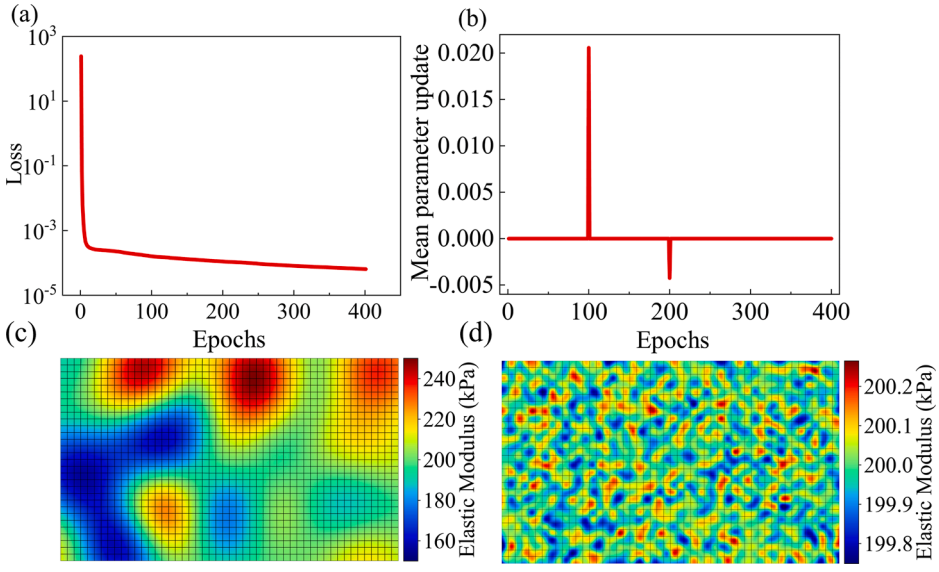


**Fig. 19.** Evaluation of direct inversion feasibility on the fine mesh: (a) loss of direct inversion on the fine mesh; (b) mean material parameters update magnitude per epoch; (c) ground truth material field in the fine mesh; (d) reconstructed material field in the fine mesh.

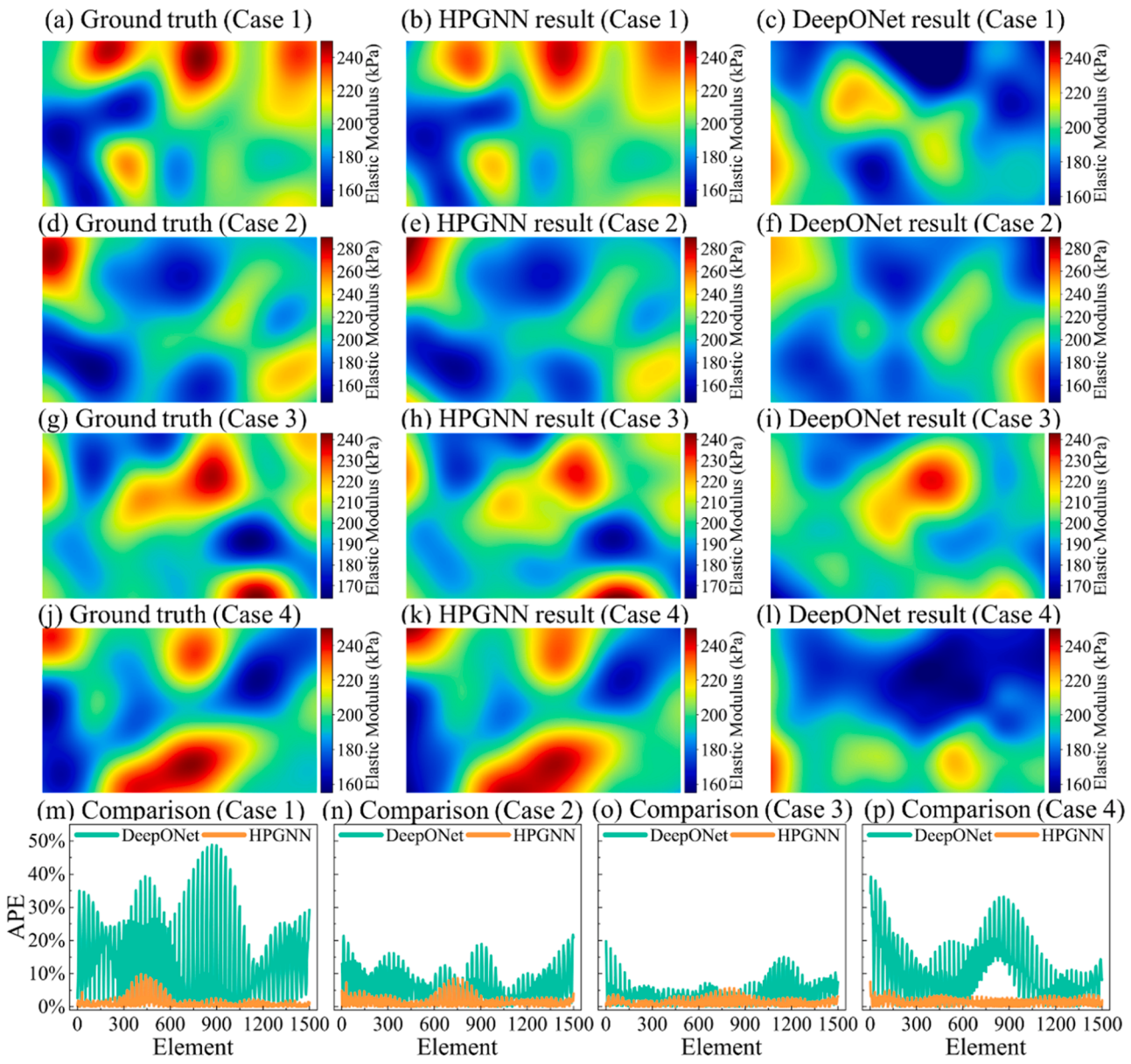


**Fig. 20.** Comparison of elastic modulus fields predicted by DeepONet and HPGNN for the elastic footing problem: (a), (d), (g), (j) four random field ground truth; (b), (e), (h), (k) HPGNN inverse results; (c), (f), (i), (l) DeepONet inverse results; Element-wise APE distributions of elastic modulus predictions obtained by DeepONet and HPGNN: (m) first random field case; (n) second random field case; (o) third random field case; (p) fourth random field case.

**Table 8**
Quantitative comparison of prediction accuracy between DeepONet and HPGNN for the elastic footing problem.

| Random field case | MAPE *of* interpolated results | |
|---|---|---|
| | DeepONet | HPGNN |
| One | 14.31 % | 1.18 % |
| Two | 6.11 % | 1.47 % |
| Three | 3.61 % | 1.32 % |
| Four | 10.82 % | 1.39 % |

Under different random field perturbations, HPGNN consistently maintains high accuracy and stability, underscoring its robustness against strong spatial variability. The investigation of extreme initial conditions shows that incorporating the LBFGS restart mechanism with properly tuned restart parameters not only improves convergence stability but also reduces computational costs, enhancing efficiency by up to 90 % compared with cases without the restart mechanism. Noise sensitivity tests also showed that, although accuracy degrades with increasing label noise, the overall error remains within an acceptable range for geotechnical inverse-analysis applications at the tested noise levels. Label data sensitivity analysis demonstrates that increasing the

number of label points continues to enhance accuracy, but with a rapidly increasing computational cost. This result highlights a fundamental trade-off between measurement density, reconstruction accuracy, and computational efficiency. Furthermore, the feasibility of direct inverse identification on fine meshes is evaluated. The results indicate that performing inverse identification directly on highly refined meshes leads to curse of dimensionality and degraded convergence, whereas the proposed hierarchical strategy effectively mitigates these issues by progressively increasing the resolution of the unknown parameter field. Finally, a direct comparison with DeepONet on the elastic footing demonstrated that purely data-driven inverse operators can suffer from higher local errors under sparse data conditions. In contrast, HPGNN leverages embedded physics constraints and hierarchical conditioning control to deliver more accurate reconstructions with improved overall efficiency in sparse data scenarios.

In summary, HPGNN offers an accurate and efficient solution for inverse problems in solid mechanics, even under the challenging initialization and sparse data labels conditions. This ability to inverse identify material properties from limited observations highlights its practical relevance in real-world engineering scenarios where dense measurement data are often costly or infeasible to obtain. By effectively bridging the gap between sparse experimental data and high-fidelity model predictions, HPGNN paves the way for broader applications across computational mechanics and engineering design, particularly in domains that demand both accuracy and efficiency in modeling strategies.

## CRediT authorship contribution statement

**Kunpeng Xu:** Writing – original draft, Validation, Software, Data curation. **Ning Zhang:** Visualization, Validation, Supervision, Software, Methodology, Funding acquisition, Conceptualization. **Zhen-Yu Yin:** Writing – review & editing, Supervision, Funding acquisition, Conceptualization. **Kai-Qi Li:** Writing – review & editing, Data curation.

## Declaration of competing interest

The authors declare that they have no known competing financial interests or personal relationships that could have appeared to influence the work reported in this paper

## Acknowledgement

This research was financially supported by the National Nature Science Foundation of China (NSFC) (Grant No. 52308377), the Research Grants Council (RGC) of Hong Kong Special Administrative Region Government (HKSARG) of China (Grant No. 15220423, E-PolyU501/24, T22-607/24-N).

## Appendix A. Interpolation of material parameters over the entire domain

To visualize and evaluate the reconstructed heterogeneous material field, a radial basis function (RBF) interpolation is employed. Using the element centers $(x_i y_i)$ and their corresponding material values $E_i$, the interpolant is constructed as below:

$$E(\boldsymbol{x},\boldsymbol{y}) = \sum_{i=1}^{N} \lambda_i \Phi(\| \boldsymbol{x} - \boldsymbol{x}_i \|),$$

where $\Phi(r)$ denotes the radial basis kernel and $\lambda_i$ are interpolation coefficients determined by enforcing exact agreement at the known data points. The cubic kernel is employed, defined as following:

$$\Phi(\boldsymbol{r}) = \boldsymbol{r}^3,$$

which yields a smooth and continuously differentiable material field without introducing additional smoothing parameters.

## Appendix B. Neural network architecture and training hyperparameters

**Table 9**
Summary of neural network architecture and training hyperparameters.

| Item | Description |
|---|---|
| Network type | ResNet |
| Number of blocks | 4 |
| Number of layers | 50 |
| Neurons per layer | 100 |
| Activation function | tanh |
| Initialization | Kaiming normal |
| Optimizer | LBFGS |
| Learning rate | 1 |
| Loss function | MSE |

## Appendix C. Results for the elastic footing under the other three random fields

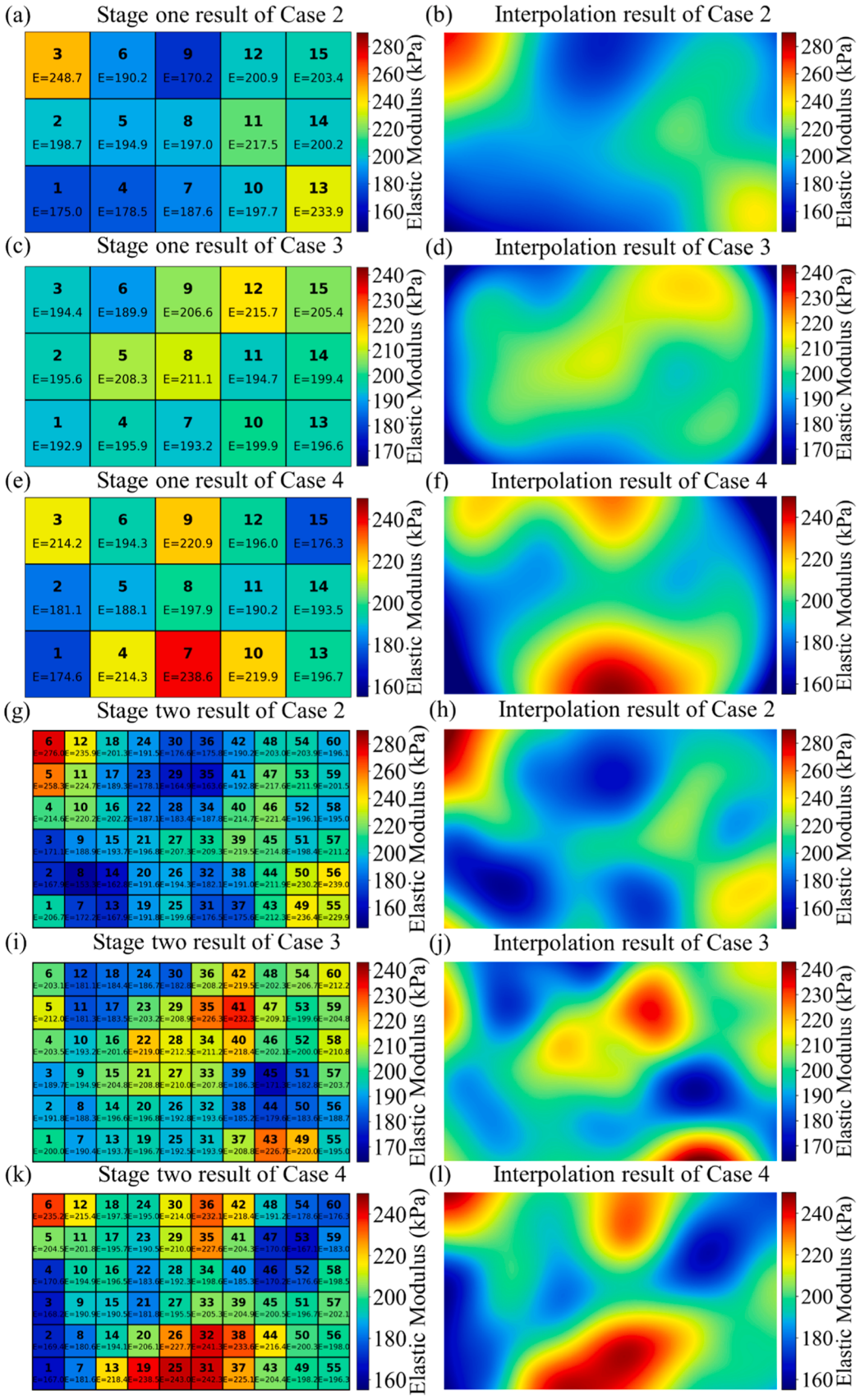


**Fig. 21.** Stage one inverse identification of elastic modulus for coarse meshes and interpolation back to fine mesh resolution for four random filed cases. (a) - (b) Case two; (c) - (d) case three; (e) - (f) case four; stage two inverse identification of elastic modulus for coarse meshes and interpolation back to fine mesh resolution for four random field cases. (g) - (h) Case two; (i) - (j) case three; (k) - (l) case four.

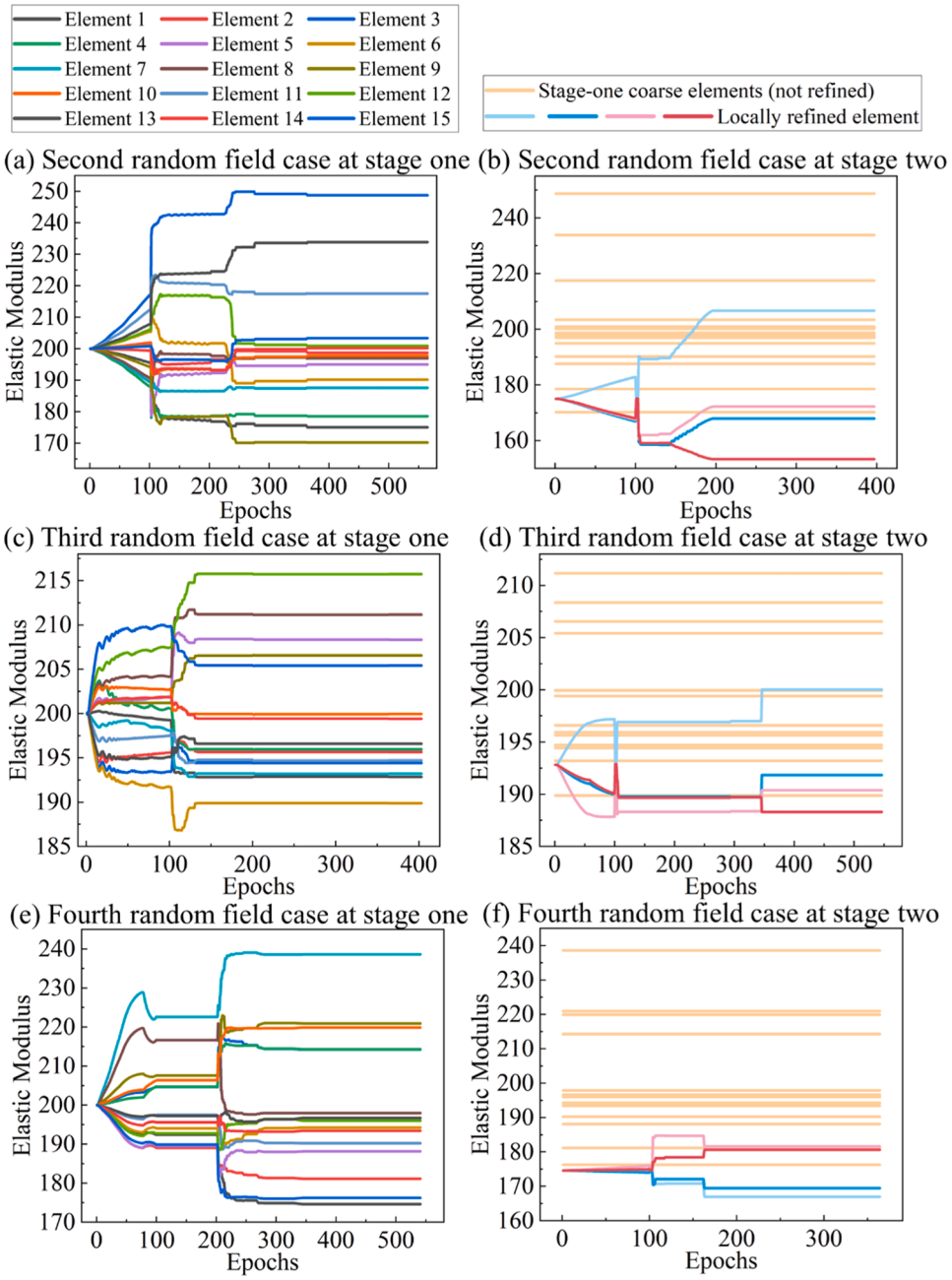


**Fig. 22.** (a), (c), (e) Convergence of element-wise elastic modulus during stage one across three random field simulations of the flexible footing. (b), (d), (f) Convergence during stage two, where only the refinement of element 1 is shown for clarity.

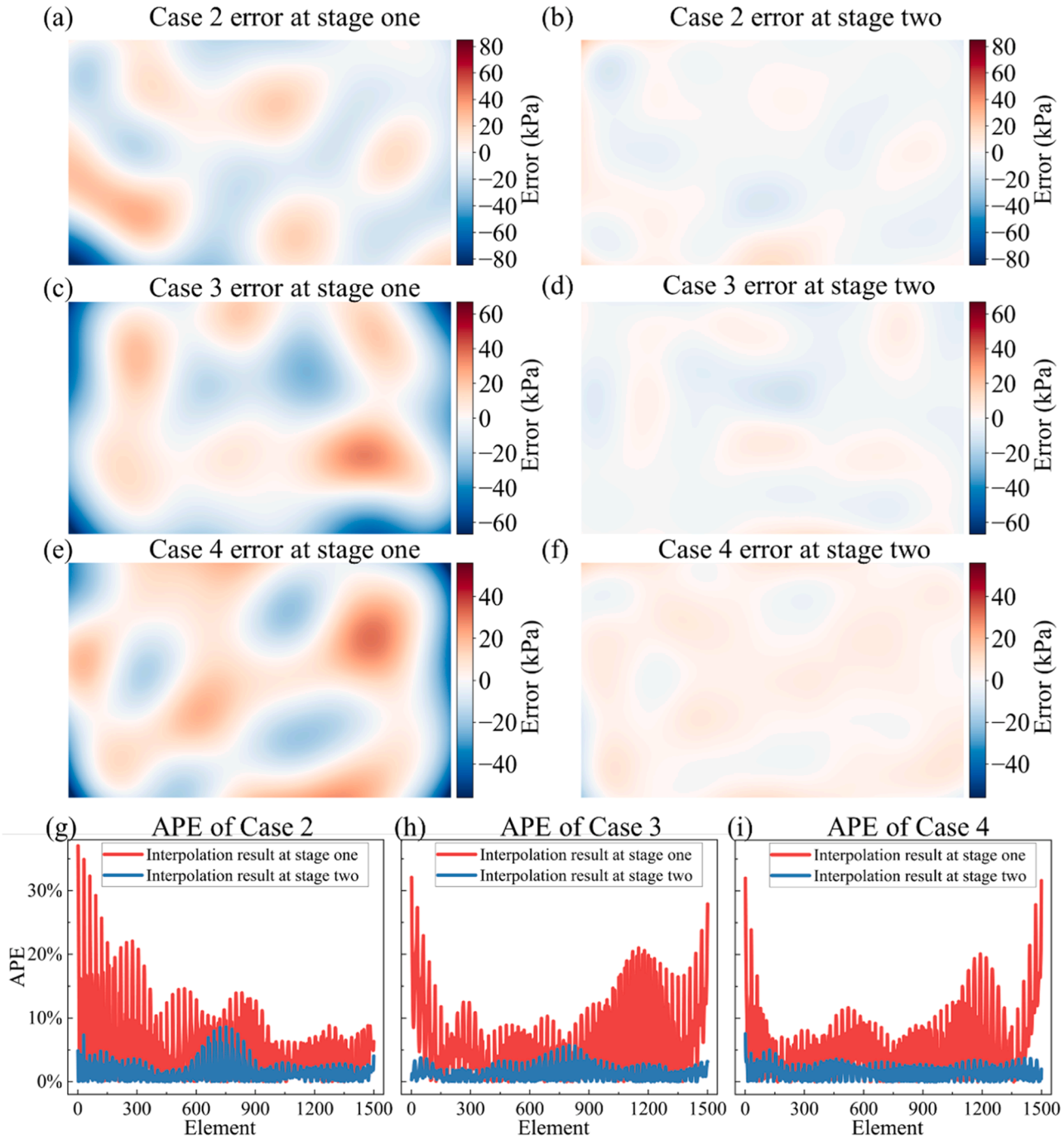


**Fig. 23.** Error analysis of the reconstructed material field: absolute error of stage-one results and absolute error of stage-two results: (a) - (b) case two; (c) – (d) case three; (e) – (f) case fourth; element-wise absolute percentage error (APE) comparison between the two stages: (g) case two; (h) case three; (i) case fourth.

## Appendix D. Discussion on multi-parameter inverse identification

In linear elastic materials, the constitutive matrix depends jointly on Young's modulus and Poisson's ratio, and different combinations of these parameters can produce nearly indistinguishable responses under identical loading and boundary conditions. As a result, inverse identification problems for linear elastic materials are inherently non-unique. To explicitly demonstrate this issue, a numerical experiment is conducted in this section, in which both Young's modulus and Poisson's ratio are prescribed as spatially varying random fields and are inversely identified simultaneously. As shown in Fig. 24(c) and (d), the reconstructed Young's modulus and Poisson's ratio fields fail to accurately capture the spatial trends of the corresponding reference fields. Quantitative results summarized in Table 10 further confirm this observation. While the reconstructed Young's modulus field achieves accuracy with a MAPE of 9.01 %, the error associated with the Poisson's ratio field increases significantly, reaching a MAPE of 25.78 %. This discrepancy highlights the intrinsic ill-posedness of simultaneous multi-parameter inverse identification in linear elasticity, rather than a limitation of the proposed framework. In this case, in the numerical examples presented in this study, Poisson's ratio is fixed to a prescribed value to ensure the well-posedness of the inverse problem. Addressing this non-uniqueness remains an important and challenging topic, and future work will focus on developing advanced strategies, such as incorporating multi-loading scenarios to reliable simultaneous identification of multiple elastic parameters.

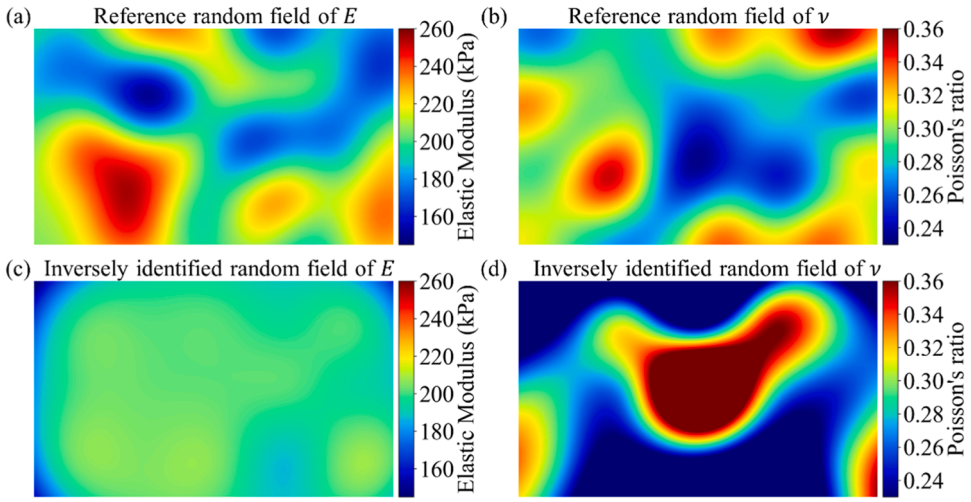


**Fig. 24.** Simultaneous inverse identification of spatially varying Young' s modulus and Poisson' s ratio: (a) reference random field of $\boldsymbol{E}$; (b) reference random field of $\boldsymbol{\nu}$; (c) inversely identified random field of $\boldsymbol{E}$; (d) inversely identified random field of $\boldsymbol{\nu}$.

**Table 10**
Inversion accuracy of Young' s modulus and Poisson' s ration.

| Trainable parameters | MAPE of interpolated results |
|---|---|
| Young' s modulus | 9.01 % |
| Poisson' s ration | 25.78 %. |

## Data availability

Data will be made available on request.

## References

[1] Tam JH, Ong ZC, Ismail Z, Ang BC, Khoo SY. Identification of material properties of composite materials using nondestructive vibrational evaluation approaches: a review. Mech Adv Mater Struct 2017;24(12):971–86.
[2] Chen B, Starman B, Halilovič M, Berglund LA, Coppieters S. Finite element model updating for material model calibration: a review and guide to practice. Arch Comput Methods Eng 2025;32(4):2035–112.
[3] Liang Y, Wei X, Peng Y, Wang X, Niu X. A review on recent applications of machine learning in mechanical properties of composites. Polym Compos 2025;46(3):1939–60.
[4] Haustrate R, Hild F, Fau A. Identifying heterogeneous elastic parameters from full-field measurements with reduced bases. Int J Mech Sci 2025:110682.
[5] Xu T, Li M, Wang Z, Hu Y, Du S, Lei Y. A direct method to identify Young's moduli and boundary conditions of the heterogeneous material. Int J Mech Sci 2025;285:109777.
[6] Qian F, Deng Y. Seismic stability of slope considering material properties and geometric characteristics. Eng Geol 2025;350:108025.
[7] Jafari MM, Bagheripour MH, Yaghoubi E. Prediction of strength properties of reinforced and stabilized sandy soil as a building foundation material. Buildings 2025;15(3):382.
[8] Wu X-H, Zhang Q, Feng W-Q, Yin Z-Y, Fang H. Enhanced THM coupling for anisotropic geomaterials and smoothed-FEM simulation. Int J Mech Sci 2025;290:110087.
[9] Souza RM, Fukumasu NK. Numerical simulation and finite element analysis. Nanomechanics for coatings and engineering surfaces. Elsevier; 2025. p. 369–92.
[10] Jin Z, Wu S-D, Yang J, Yin Z-Y, Chen X. Failure mechanism of suction anchor based on FEM-SPH method considering torsion effect. Ocean Eng 2025;332:121408.
[11] Lee H-R, Lee M-G, Park N. Effect of evolutionary anisotropic hardening on the prediction of deformation and forming load in incremental sheet forming simulation. Thin-Wall Struct 2023;193:111231.
[12] Rizzieri G, Ferrara L, Cremonesi M. Numerical simulation of the extrusion and layer deposition processes in 3D concrete printing with the Particle finite element method. Comput Mech 2024;73(2):277–95.
[13] Zhu P, Yang S, Gao Z, Liu J, Zhou L. Optimization of hot deformation parameters for multi-directional forging of Ti65 alloy based on the integration of processing maps and finite element method. J Mater Res Technol 2024;29:5271–81.
[14] Yin Z-Y. Three-dimensional numerical modelling of progressive failure of caisson foundation in sand using a coupled FDM–DEM method. Ocean Eng 2022;253:111332.
[15] Eskandari Z, Avazzadeh Z, Ghaziani RK, Li B. Dynamics and bifurcations of a discrete-time Lotka–Volterra model using nonstandard finite difference discretization method. Math Methods Appl Sci 2025;48(7):7197–212.
[16] Raza Q, Wang X, Ali B, Li S, Shah NA, Yang H. Computational study on entropy generation in Casson nanofluid flow with motile gyrotactic microorganisms using finite difference method. Chaos Solit Fract 2025;190:115758.
[17] Boudjedour A, Batiha I, Boucetta S, Dalah M, Zennir K, Ouannas A. A finite difference method on uniform meshes for solving the time-space fractional advection-diffusion equation. Gulf J Mathe 2025;19(1):156–68.
[18] Lin D, Gao L, Gao J. The Lagrangian-Eulerian described particle flow topology optimization (PFTO) approach with isogeometric material point method. Comput Methods Appl Mech Eng 2025;440:117892.
[19] He KY, Jin YF, Zhou XW, Yin ZY, Chen X. A multi-resolution material point method based on penalty formulation. Int J Numer Anal Methods Geomech 2025.
[20] Siron M, Trottet B, Gaume J. A theoretical framework for dynamic anticrack and supershear propagation in snow slab avalanches. J Mech Phys Solids 2023;181:105428.
[21] Telikicherla RM, Moutsanidis G. An assessment of the total Lagrangian material point method: comparison to conventional MPM, higher order basis, and treatment of near-incompressibility. Comput Methods Appl Mech Eng 2023;414:116135.
[22] Hu Z, Liu Y, Zhang Z, Ye H, Zhang H, Zheng Y. Coupling explicit phase-field MPM for two-dimensional hydromechanical fracture in poro-elastoplastic media. Int J Mech Sci 2023;260:108649.
[23] Pan J-h, Pinzón G, Wang R, Andò E, Viggiani G, Zhang J-M. Lessons learned from matching 3D DEM and experiments at macro, meso and fabric scales for triaxial compression tests on lentils. J Mech Phys Solids 2024;183:105494.
[24] Wagner JJ, Higgs III CF. Coupled CFD-DEM simulation of interfacial fluid–particle interaction during binder jet 3D printing. Comput Methods Appl Mech Eng 2024;421:116747.
[25] Su Z, Xu C, Jia K, Cui C, Du X. A novel semi-resolved CFD-DEM coupling method based on point cloud algorithm for complex fluid-particle systems. Comput Methods Appl Mech Eng 2025;434:117561.
[26] Zhang X, Yang Y, Xu F. A combined finite-discrete element model for elasto-capillary phenomena. Int J Mech Sci 2023;251:108305.
[27] Cheng T, Meng Z, Liu W, Li J, Liu J, Huang S. Inverse identification of constitutive model for metallic thin sheet via electromagnetic hydraulic bulge experiment. Int J Mater Form 2023;16(4):38.
[28] Conde M, Zhang Y, Henriques J, Coppieters S, Andrade-Campos A. Design and validation of a heterogeneous interior notched specimen for inverse material parameter identification. Fin Elem Anal Des 2023;214:103866.

[29] Won JY, Kim C, Hong S, Yoon H-S, Park JK, Lee M-G. Evaluation of crush performance of extruded aluminum alloy tubes based on finite element analysis with ductile fracture modeling. Thin-Wall Struct 2024;200:111937.
[30] Givoli D. A tutorial on the adjoint method for inverse problems. Comput Methods Appl Mech Eng 2021;380:113810.
[31] Badia S, Li W, Martín AF. Finite element interpolated neural networks for solving forward and inverse problems. Comput Methods Appl Mech Eng 2024;418:116505.
[32] Zhou A, Farimani AB. Predicting change, not states: an alternate framework for neural PDE surrogates. Comput Methods Appl Mech Eng 2025;441:117990.
[33] Xu T, Liu D, Hao P, Wang B. Variational operator learning: a unified paradigm marrying training neural operators and solving partial differential equations. J Mech Phys Solids 2024;190:105714.
[34] Li KQ, Yin ZY. Relative ice saturation and unified elastoplastic modeling of frozen soils. J Geotech Geoenviron Eng 2025;151(12):04025150.
[35] Li KQ, Yin ZY, Qi JL, Liu Y. State-of-the-art constitutive modelling of frozen soils. Arch Comput Method Eng 2024;31(7):3801–42.
[36] Li KQ, Yin ZY, Zhang N, Liu Y. A data-driven method to model stress-strain behaviour of frozen soil considering uncertainty. Cold Reg Sci Technol 2023;213:103906.
[37] Jin Z, Zhang W, Yin Z-Y, Zhang N, Geng X. Estimating track geometry irregularities from in-service train accelerations using deep learning. Autom Construct 2025;173:106114.
[38] Zhang H, Yin Z-Y, Zhang N, Wang X. Self-supervised transformer for 3D point clouds completion and morphology evaluation of granular particle. Appl Soft Comput 2025;176:113161.
[39] Xu H-R, Yin J-N, Zhang N. Transformer-based deformation measurement of underground structures from a single-camera video. Autom Construct 2025;172:106070.
[40] Hao W, Shi D, Yang X, Li N, Su S, Fan Y. Multi-mode fatigue life prediction using machine learning inspired by damage physics. Int J Mech Sci 2025:110723.
[41] Li KQ, Yin ZY, Liu Y. AGFNN: A smart platform for uncertainty-aware prediction of freezing time in artificial ground freezing. Tunn Undergr Space Tech 2026;170:107331.
[42] Wang Y, et al. A physics-informed deep learning framework for solving forward and inverse problems based on Kolmogorov–Arnold Networks. Comput Methods Appl Mech Eng 2025;433:117518.
[43] Wang Y, et al. Kolmogorov–Arnold-informed neural network: a physics-informed deep learning framework for solving forward and inverse problems based on Kolmogorov–Arnold Networks. Comput Methods Appl Mech Eng 2025;433:117518.
[44] Zhuang X, Tran TV, Nguyen-Xuan H, Rabczuk T. Deep learning-based post-earthquake structural damage level recognition. Comput Struct 2025;315:107761.
[45] Zhang N, Shen S-L, Wu H-N, Chai J-C, Xu Y-S, Yin Z-Y. Evaluation of effect of basal geotextile reinforcement under embankment loading on soft marine deposits. Geotext Geomembr 2015;43(6):506–14.
[46] Xu H-R, Zhang N, Yin Z-Y, Njock PGA. Multimodal framework integrating multiple large language model agents for intelligent geotechnical design. Autom Construc 2025;176:106257.
[47] Xu H-R, Zhang N, Yin Z-Y, Njock PGA. GeoLLM: a specialized large language model framework for intelligent geotechnical design. Comput Geotechn 2025;177:106849.
[48] Yan T, Shen S-L, Yin Z-Y, Zhang N. Multi-source data-driven prediction of geological cross-section during shield tunnelling. Autom Construc 2026;181:106592.
[49] Njock PGA, Yin Z-Y, Xu H-R, Zhang N. Structural failure risk assessment of shield tunnel using large language model. Tunnell Undergr Space Technol 2025;165:106882.
[50] Li K-Q, Yin Z-Y, Zhang N, Liu H-C. Physics-informed neural networks for solving steady-state temperature field in artificial ground freezing. Can Geotechn J 2025;62:1–17.
[51] Li K-Q, Yin Z-Y, Zhang N, Li J. A PINN-based modelling approach for hydromechanical behaviour of unsaturated expansive soils. Comput Geotechn 2024;169:106174.
[52] Xu K, Zhang N, Yin Z-Y, Li K. Finite element-integrated neural network for inverse analysis of elastic and elastoplastic boundary value problems. Comput Methods Appl Mech Eng 2025;436:117695.
[53] Zhang N, Zhou A, Jin Y-F, Yin Z-Y, Shen S-L. An enhanced deep learning method for accurate and robust modelling of soil stress–strain response. Acta Geotechn 2023;18(8):4405–27.
[54] Zhang N, Shen S-L, Zhou A, Jin Y-F. Application of LSTM approach for modelling stress–strain behaviour of soil. Appl Soft Comput 2021;100:106959.
[55] Alzubaidi L, et al. A survey on deep learning tools dealing with data scarcity: definitions, challenges, solutions, tips, and applications. J Big Data 2023;10(1):46.
[56] Raissi M, Perdikaris P, Karniadakis GE. Physics-informed neural networks: a deep learning framework for solving forward and inverse problems involving nonlinear partial differential equations. J Comput Phys 2019;378:686–707.
[57] Zhang N, Xu K, Yin ZY, Li K-Q, Jin Y-F. Finite element-integrated neural network framework for elastic and elastoplastic solids. Comput Methods Appl Mech Eng 2025;433:117474.
[58] Zhang N, Xu K, Yin Z-Y, Li K-Q. Transfer learning-enhanced finite element-integrated neural networks. Int J Mech Sci 2025;290:110075.
[59] Bi H, Song M, Zhang T, Liu X. FC-PINNs: physics-informed neural networks for solving neutron diffusion eigenvalue problem with interface considerations. J Comput Phys 2025:114311.
[60] Liang R, Liu W, Xu L, Qu X, Kaewunruen S. Solving elastodynamics via physics-informed neural network frequency domain method. Int J Mech Sci 2023;258:108575.
[61] Cheng Z, Yu T, Jia G, Shi Z. A physics-informed neural network-based method for dispersion calculations. Int J Mech Sci 2025;291:110111.
[62] Liu C-X, Wang X, Liu W, Yang Y-F, Yu G-L, Liu Z. A physics-informed neural network for Kresling origami structures. Int J Mech Sci 2024;269:109080.
[63] Karnakov P, Litvinov S, Koumoutsakos P. Solving inverse problems in physics by optimizing a discrete loss: fast and accurate learning without neural networks. PNAS Nexus 2024;3(1):pgae005.
[64] Wang F, Zhai W, Zhao S, Man J. A novel unsupervised PINN framework with dynamically self-adaptive strategy for solid mechanics. J Comput Phys 2025:114373.
[65] Xiong Z, Yang P, Zhao P. Physics-driven neural networks for nonlinear micromechanics. Int J Mech Sci 2024;273:109214.
[66] Wei C, Fan Y, Wong JC, Ooi CC, Wang H, Chiu P-H. FFV-PINN: a fast physics-informed neural network with simplified finite volume discretization and residual correction. Comput Methods Appl Mech Eng 2025;444:118139.
[67] Liu Y, Park C, Lu Y, Mojumder S, Liu WK, Qian D. HiDeNN-FEM: a seamless machine learning approach to nonlinear finite element analysis. Comput Mech 2023;72(1):173–94.
[68] Jiang Q, Shu C, Zhu L, Yang L, Liu Y, Zhang Z. Applications of finite difference-based physics-informed neural networks to steady incompressible isothermal and thermal flows. Int J Numer Methods Fluids 2023;95(10):1565–97.
[69] Haghighat E, Raissi M, Moure A, Gomez H, Juanes R. A physics-informed deep learning framework for inversion and surrogate modeling in solid mechanics. Comput Methods Appl Mech Eng 2021;379:113741.
[70] Guo H, Yin Z-Y. A novel physics-informed deep learning strategy with local time-updating discrete scheme for multi-dimensional forward and inverse consolidation problems. Comput Methods Appl Mech Eng 2024;421:116819.
[71] Xu C, Cao BT, Yuan Y, Meschke G. Transfer learning based physics-informed neural networks for solving inverse problems in engineering structures under different loading scenarios. Comput Methods Appl Mech Eng 2023;405:115852.
[72] Motlagh YG, Fathi F, Brigham JC, Jimack PK. Deep learning for inverse material characterization. Comput Methods Appl Mech Eng 2025;436:117650.
[73] Mika ML, Hughes TJ, Schillinger D, Wriggers P, Hiemstra RR. A matrix-free isogeometric Galerkin method for Karhunen–Loève approximation of random fields using tensor product splines, tensor contraction and interpolation based quadrature. Comput Methods Appl Mech Eng 2021;379:113730.
[74] Hong S, Kim H, Lee M-G. Anisotropic plasticity identification: integrated FE and sensitivity-based virtual fields method. Int J Mech Sci 2025:110815.
[75] Zou Z, He L, Zhou T, Zhang W, Tian P, Zhou X. Research on inverse identification of Johnson-Cook constitutive parameters for turning 304 stainless steel based on coupling simulation. J Mater Res Technol 2023;23:2244–62.
[76] Lee J, et al. Machine learning-based inverse design methods considering data characteristics and design space size in materials design and manufacturing: a review. Mater Horiz 2023;10(12):5436–56.
[77] Khosrozadeh A, Khosravifard A, Rajabi I. Inverse identification of material constants of various cohesive laws for delamination of composites using experimental results. Compos Struct 2023;303:116241.
[78] Tariq A, Deliktaş B. An inverse parameter identification in finite element problems using machine learning-aided optimization framework. Exp Mech 2025;65(3):325–49.
[79] Pandey A, Bhandari L, Gaur V. Identification and optimization of material constitutive equations using genetic algorithms. Eng Appl Artif Intell 2024;128:107534.
[80] van der Heijden B, Li X, Lubineau G, Florentin E. Enforcing physics onto PINNs for more accurate inhomogeneous material identification. Comput Methods Appl Mech Eng 2025;441:117993.
[81] Wang H, Zhou W, Wang H, Li G. A DeepONets-based resolution independent ABC inverse method for determining material parameters of HAZ. Eng Fract Mech 2025;315:110843.
[82] Jiang X, Wang X, Wen Z, Wang H. Resolution-independent generative models based on operator learning for physics-constrained Bayesian inverse problems. Comput Methods Appl Mech Eng 2024;420:116690.
[83] Jiang X, Wang X, Wen Z, Li E, Wang H. Practical uncertainty quantification for space-dependent inverse heat conduction problem via ensemble physics-informed neural networks. Int Commun Heat Mass Transf 2023;147:106940.
[84] Wang X, Zeng Y, Wang H, Cai Y, Li E, Li G. Data-driven inverse method with uncertainties for path parameters of variable stiffness composite laminates. Struct Multidiscipl Optimiz 2022;65(3):91.
[85] Meng X, Karniadakis GE. A composite neural network that learns from multi-fidelity data: application to function approximation and inverse PDE problems. J Comput Phys 2020;401:109020.
[86] Yang S, Lin K, Zhou A. Evaluating water retention and hydraulic conductivity properties based on the Richardson–Richards equation using progressive training and trainable weights. Int J Numer Anal Methods Geomech 2025.
[87] Yang J, Liu X, Diao Y, Chen X, Hu H. Adaptive task decomposition physics-informed neural networks. Comput Methods Appl Mech Eng 2024;418:116561.
[88] Kapoor T, Wang H, Núñez A, Dollevoet R. Physics-informed neural networks for solving forward and inverse problems in complex beam systems. IEEE Trans Neural Netw Learn Syst 2023;35(5):5981–95.

[89] Shukla K, Zou Z, Chan CH, Pandey A, Wang Z, Karniadakis GE. NeuroSEM: a hybrid framework for simulating multiphysics problems by coupling PINNs and spectral elements. Comput Methods Appl Mech Eng 2025;433:117498.
[90] Wang S, Teng Y, Perdikaris P. Understanding and mitigating gradient flow pathologies in physics-informed neural networks. SIAM J Sci Comput 2021;43(5): A3055–81.
[91] Mattey R, Ghosh S. A novel sequential method to train physics informed neural networks for Allen Cahn and Cahn Hilliard equations. Comput Methods Appl Mech Eng 2022;390:114474.
[92] G. Zhang, H. Yang, F. Zhu, and Y. Chen, "Dasa-pinns: differentiable adversarial self-adaptive pointwise weighting scheme for physics-informed neural networks," 2023.
[93] W. Chen, A.A. Howard, and P. Stinis, "Self-adaptive weights based on balanced residual decay rate for physics-informed neural networks and deep operator networks," *arXiv preprint arXiv:2407.01613,* 2024.
[94] Rao Y, Wang Y. Seismic waveform tomography with shot-encoding using a restarted L-BFGS algorithm. Sci Rep 2017;7(1):8494.
[95] Byrd RH, Hansen SL, Nocedal J, Singer Y. A stochastic quasi-newton method for large-scale optimization. SIAM J Optimiz 2016;26(2):1008–31.
[96] Liu Y, Li J, Sun S, Yu B. Advances in Gaussian random field generation: a review. Comput Geosci 2019;23(5):1011–47.
[97] Uribe F, Papaioannou I, Betz W, Straub D. Bayesian inference of random fields represented with the Karhunen–Loève expansion. Comput Methods Appl Mech Eng 2020;358:112632.
[98] J. Doob, "Michel Loève, probability theory," 1961.
[99] Ghanem RG, Spanos PD. Stochastic finite element method: response statistics. Stochastic finite elements: a spectral approach. Springer; 1991. p. 101–19.
[100] Le Maître O, Knio OM. Spectral methods for uncertainty quantification: with applications to computational fluid dynamics. Springer Science & Business Media; 2010.
[101] He K, Zhang X, Ren S, Sun J. Deep residual learning for image recognition. In: Proceedings of the IEEE conference on computer vision and pattern recognition; 2016. p. 770–8.
[102] Guo H, Zhuang X, Chen P, Alajlan N, Rabczuk T. Stochastic deep collocation method based on neural architecture search and transfer learning for heterogeneous porous media. Eng Comput 2022;38(6):5173–98.
[103] Sahin T, von Danwitz M, Popp A. Solving forward and inverse problems of contact mechanics using physics-informed neural networks. Adv Model Simul Eng Sci 2024;11(1):11.
[104] Pottier L, Thorin A, Chinesta F. Latent-energy-based NNs: an interpretable neural network architecture for model-order reduction of nonlinear statics in solid mechanics. J Mech Phys Solids 2025;194:105953.